Applications in Energy and Combustion Science 27 (2026) 100519

Contents lists available at ScienceDirect

Applications in Energy and Combustion Science

journal homepage: www.elsevier.com/locate/jaecs

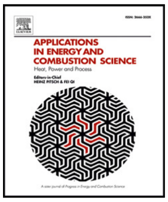

Additive manufacturing enabled annular µ-slit injection in low NO_X jet-stabilised liquid fuel combustion

Yeonse Kang [a], Oliver Lammel [b], Matthias Ruf [c], Holger Steeb [c,d], Hans-Christian Möhring [e], Fabian Hampp [a,*]

[a] *Institute of Combustion Technology for Aerospace Engineering (IVLR), University of Stuttgart, Stuttgart, Germany*
[b] *German Aerospace Center (DLR), Institute of Combustion Technology, Stuttgart, Germany*
[c] *Institute of Applied Mechanics (MIB), University of Stuttgart, Stuttgart, Germany*
[d] *Stuttgart Center for Simulation Science (SC SimTech), University of Stuttgart, Stuttgart, Germany*
[e] *Institute for Machine Tools (IfW), University of Stuttgart, Stuttgart, Germany*

ARTICLE INFO

Keywords:
Additive manufacturing
Annular µ-slit injector
Spray atomisation
Jet-stabilised combustion
Micro gas turbine
Hybrid aero-engine concept

ABSTRACT

Advanced fuel injection systems are vital for improving combustion performance and reducing emissions in liquid-fuel-powered, high-momentum jet-stabilised combustion systems. This paper introduces an additively manufactured (AM) µ-scale annular slit injector with a nominal gap width of 50 µm, realised by laser powder bed fusion in Inconel 718. µ-XRCT measurements confirm a manufacturable width of 52 µm and reveal a transition towards statistically isotropic circumferential discharge at the slit exit. Compared with conventional dual airblast injection (AB), the µ-slit topology generates more uniformly fine droplets ($d_{32} \approx 10\,\mu m$) and a markedly reduced radial asymmetry in fuel placement. The homogenised annular fuel discharge suppresses sectional bias and intermittency at the nozzle edge while enhancing fuel–air mixing, redistributing clustering length scales, and promoting more robust combustion across variations in jet velocity and fuel loading. Structural variants, e.g., µ-bumps and a low-swirler configuration, further modulate near-field multi-phase interaction and flame anchoring while enhancing overall flame homogeneity. This mixing-optimised stabilisation enhances the symmetry of the OH^*-marked heat-release structures and enables stable low-NO_X combustion under lean atmospheric conditions. The injector operates with a comparatively low pressure drop with excellent reproducibility across all investigated mass flow rates, facilitating a wide dynamic operating range, yet heat transfer within the µ-channels under elevated preheating conditions requires further investigation. These results establish the AM µ-slit injector as a scalable low-emission architecture for compact, jet-stabilised micro gas turbine and hybrid aero-engine combustors.

1. Introduction

As renewable energy sources increasingly penetrate the global energy mix on the pathway towards a decarbonised society, the establishment of robust transition strategies that couple existing power-generation infrastructure with zero-carbon technologies has become imperative [1]. The rapid growth of energy-intensive digital infrastructure, including large-scale data centres and high-performance computing facilities driven by artificial intelligence workloads, further amplifies the demand for reliable, dispatchable, and high power-density energy systems [2–4]. Within this framework, gas turbine (GT) systems represent a mature yet adaptable platform capable of accommodating a broad range of carbon-neutral fuels, including hydrogen (H_2), ammonia (NH_3), bio-derived fuels, and sustainable aviation fuels (SAF), across power generation, transportation, and industrial applications [5–7]. However, the ongoing diversification of chemical energy carriers imposes stringent requirements on GTs and other thermo-chemical conversion systems, necessitating the optimisation of fuel delivery and injection hardware to ensure high fuel flexibility and scalability, while simultaneously minimising cost, maximising efficiency, and reducing emissions. In this context, additive manufacturing has

---

* Corresponding author.
E-mail address: fabian.hampp@ivlr.uni-stuttgart.de (F. Hampp).

https://doi.org/10.1016/j.jaecs.2026.100519
Received 25 March 2026; Received in revised form 15 May 2026; Accepted 28 May 2026

Nomenclature

ΔP	Pressure drop across fuel injector
Δ_{vox}	Voxel size
$\dot{m}_{f,lc}$	Local fuel feeding rate
$\dot{m}_l$	Liquid fuel mass flow rate
μ	Dynamic viscosity
ν	Kinematic viscosity
Φ	Equivalence ratio
ψ	Normalised cross-correlation coefficient
ρ	Density
σ	Surface tension
A_{asym}	Flame area asymmetry
d	Droplet diameter
d_{10}	Arithmetic mean droplet diameter
d_{32}	Sauter mean droplet diameter
D_c	Combustor nozzle inner diameter
$D_{w1,d}$	Wasserstein distance of droplet size
$D_{w1,f}$	Wasserstein distance of local fuel feeding rate
$D_{w1,I}$	Wasserstein distance of OH* intensity
G_c	Classical cluster-resolved group combustion number
G_v	Voronoi-based cluster-resolved group combustion number
H_m	Height of μ-structure
H_N	Normalised angular entropy
I_p	Intensity population of μ-XRCT image
$I_{\max}$	Maximum OH*-CL intensity
$I_{i,j}$	Instantaneous OH* intensity at pixel (i, j)
k	Turbulence kinetic energy
$l_{\max}$	Axial location of maximum OH* intensity
L_c	Characteristic cluster length scale
L_i	Inter-droplet spacing
l_{loh}	Flame lift-off height
l_{ov}	Axial length of the outer vanes
L_p	Probe length scale
l_r	Axial distance of the outer vanes from the AB edge
l_{wf}	Wall-film length
Le	Lewis number
n_j	Number of radial pixels
n_T	Cluster number-density parameter
Oh	Ohnesorge number
Re_d	Droplet Reynolds number
Re_s	Slip Reynolds number
S	Non-dimensional droplet separation
Sc	Schmidt number
t_a	Inter-droplet arrival time
T_j	Air preheating temperature
t_s	Slit gap thickness
u_j	Air jet bulk velocity
u_x	Radial velocity component
u_y	Circumferential velocity component
$u_{z,s}$	Axial slip velocity
u_z	Axial velocity component
We_s	Slip Weber number
x	Radial coordinate
y	Circumferential coordinate
z	Axial coordinate

AB	Airblast
AM	Additively manufactured
CL	Chemiluminescence
GT	Gas turbine
HMJC	High-momentum jet-stabilised combustion
MGT	Micro gas turbine
OH*–CL	Hydroxyl chemiluminescence
PDI	Phase Doppler interferometry
PJSB	Piloted jet spray burner
PS	Pressure-swirl injector

emerged as an enabling technology for advanced GT hardware, offering design freedom for complex, flow-optimised geometries with reduced assembly constraints and potential reductions in material usage and manufacturing cost [8–10].

In practical burner applications, this design freedom enables novel geometries that integrate turbulence-generating structures with fuel injection features to influence mixing and stabilisation processes, beyond the constraints of conventional manufacturing. For turbulence tuning on gas-phase fuel and air concepts, Giuliani et al. demonstrated that additively manufactured (AM) swirler designs can outperform their conventionally manufactured counterparts, particularly under lean operating conditions approaching the flammability limit [11]. Rajasegar et al. reported AM meso-scale combustors for premixed CH_4 flames stabilised by swirling jets, achieving superior power density, combustion performance, and emission characteristics compared to macro-scale configurations [12]. Extending these concepts to smaller scales, Kim et al. reviewed the development of AM-based micro-mix burners for aero-engine applications with hydrogen premixed combustion, highlighting substantial performance gains achieved through combined numerical optimisation and experimental validation [13]. For accommodating various gaseous fuels, Durocher et al. introduced an AM micro-mix nozzle capable of operating with fuels from pure CH_4 to H_2, demonstrating stable combustion across various mixing concepts with high fuel flexibility, broad stability limits, and low susceptibility to combustion instabilities [14]. Recent advances further demonstrate that AM space-filling injector micro-structures can decouple mixture formation from fuel properties, thereby promoting homogeneous mixing prior to flame interaction [15]. Collectively, these studies show that additive manufacturing expands the design space for controlling fuel-air mixing and stabilisation in gaseous combustion systems.

Despite advances in fuel and flow modulation, the application of additive manufacturing to liquid fuel injectors faces significant challenges in achieving effective atomisation, which directly governs evaporation and combustion performance. These challenges include achieving nozzle dimensions below 200 μm for MGT applications, maintaining manufacturing tolerances within single-digit micrometres, and understanding the effects of surface roughness to mitigate flow disturbances and coking tendencies. Guddati et al. emphasised the difficulty of creating structures with feature sizes smaller than 100 μm using additive manufacturing, identifying it as a significant limitation [16]. Crayford et al. [17] investigated AM airblast (AB) liquid atomisers by analysing droplet size distributions and highlighted surface roughness as a potential factor affecting performance. Additionally, Adamou et al. evaluated an AM fuel vaporisation injector featuring 200 μm holes through numerical and experimental approaches, demonstrating more complex combustion behaviour [18]. Nonetheless, overcoming these manufacturing challenges and rigorously assessing extreme design solutions are essential to enable injector concepts that decouple fuel-air mixing from intrinsic fuel properties, thereby facilitating seamless operation across both gaseous and liquid fuels without requiring structural modifications [15,19].

Slit-shaped channels have been investigated across a broad spectrum of propulsion and combustion applications, including internal [20], combustion engines [21], rocket and detonation thrusters [22], and flashback [23] and leakage studies [24] for both liquid and gaseous fuels, owing to their precise injection, area control, simple and compact design, modular scalability, and uniform stress distribution. In the GT context, single-slit configurations with widths between 0.6 mm and 2 mm have been utilised with H_2/air premixed flames to establish global flashback thresholds and develop empirical correlations [25]. Lee and Kim further demonstrated flashback resilience of H_2/air premixed flames and thermoacoustic dynamics using a 1.5 mm multi-slit injector under GT-relevant conditions [26]. Moving to liquid-fuel systems, Lefebvre introduced a prefilming air-blast slit injector that spreads fuel into a thin film for rapid atomisation [27]. Subsequent pioneering work by Sattelmayer and Wittig examined the effects of fluid viscosity and surface-tension on atomisation characteristics under atmospheric conditions [28,29]. Bhayaraju and Hassa later extended this concept by investigating 0.3 mm slit geometries in both prefilming and non-prefilming AB atomisers under elevated pressure and velocity conditions [30]. Kumar and Sahu then characterised jet-breakup modes in coaxial AB injectors with 1.5 mm slits, correlating regime shifts with aerodynamic Weber number and momentum flux ratio [31]. Despite these advances, producing sub-millimetre slit widths capable of generating intrinsic micrometre-scale liquid films ($\leq 100\,\mu$m) remains beyond the reach of conventional machining. Consequently, the fundamental interaction between such ultra-fine, swirl-free liquid films and high-momentum jets under GT-relevant conditions has not been systematically investigated, although mixing and flame anchoring in such flows are governed by jet-induced shear, turbulent entrainment, and momentum flux interactions.

High-momentum jet-stabilised combustion (HMJC) systems are well suited for a diverse fuel market, from 100% hydrogen (H_2) to extra-light heating oil, while maintaining low non-CO_2 emissions through enhanced jet-shear layer mixing and distributed reaction zones [32–34]. The approach has been successfully scaled to micro gas turbines (MGT) with gaseous fuels [35,36] and applied in configurations ranging from industrial furnace burners to aero-engine combustor concepts [37,38]. Realising liquid fuel-based jet-stabilised combustion requires optimised spray atomisation and homogeneous fuel-air mixing to minimise non-CO_2 emissions, particularly NO_X and particulate matter. Recent studies have demonstrated the scalability and fuel flexibility of liquid-fuel jet-stabilised combustors using dual AB injectors [34,39–41]. However, when a hollow-cone spray is integrated into an AB wall configuration for prefilming, its atomisation behaviour is governed by the internal injector geometry, i.e., tangential or axial inlet ports, a swirl chamber, converging passages, and an exit orifice, which induce strong angular momentum and pressure gradients within the nozzle [42–45]. In addition, the injector itself acts as a bluff body to the external flow, further contributing to the rise of local velocity gradients and coherent flow structures [46–48]. These flow structures can suppress radial fuel dispersion and secondary atomisation, generating complex recirculation zones and local stagnation regions. The resulting droplet clustering and mixture stratification, which become most prominent during part-load operation, lead to non-uniform evaporation rates and heat-release distributions, thereby degrading combustion efficiency, compromising flame stability, and increasing NO_X and unburnt hydrocarbon (UHC) emissions. To address these drawbacks, fuel-air mixing lengths and injection positions have been systematically varied under different fuel properties and operating conditions [34,41]. Dual AB schemes achieve rapid primary atomisation and yield NO_X and CO emissions comparable to those in premixed methane fuelled systems. Meanwhile, low circumferential forcing has been introduced to enhance fuel-air mixing uniformity and flame stabilisation [40,47,49], thereby reducing droplet size, broadening radial fuel dispersion, shortening flame length, and lowering emissions. However, deploying dual AB injectors with additional structural modulations in densely packed multi-nozzle arrays for high-momentum jet-stabilised combustion systems in MGTs and future hybrid aero-engine concepts introduces substantial challenges in terms of scalability and operational complexity.

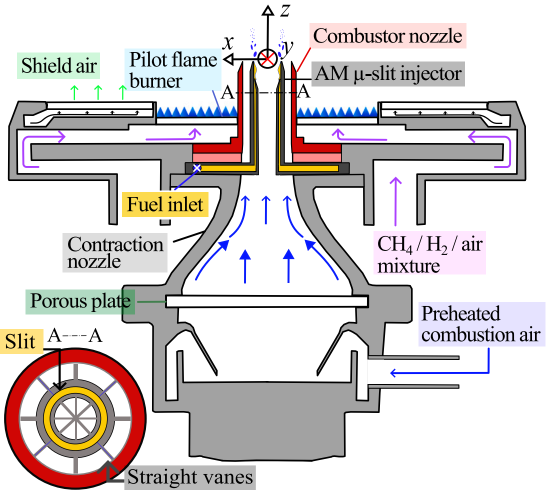

Fig. 1. Schematic of the developed single-nozzle piloted jet spray burner (PJSB), with arrows indicating the liquid and gaseous flow directions. The individual components are colour-coded for clarity. The coordinate system origin is located at the centre of the combustor nozzle exit. Section A–A illustrates the annular configuration of the additively manufactured (AM) μ–slit injector integrated at the centre of the combustor nozzle.

To overcome these limitations, we depart from conventional dual AB-based atomisation concepts and introduce an AM μ-scale annular slit injector that pushes the liquid fuel discharge scale below 100 μm, generating a swirl-free, ultra-thin annular liquid film for shear-driven atomisation in a high-momentum jet. The geometric fidelity of the nominal 50 μm slit is verified using micro X-ray computed tomography (μ-XRCT). The study examines how the microscale annular film redistributes droplet size and fuel placement, and how it influences reaction-zone structure and flame anchoring in jet momentum-dominated flows across different injector configurations. Droplet-laden flow fields are characterised using shadowgraphy and phase Doppler interferometry (PDI), while combustion dynamics are analysed via time-resolved OH* chemiluminescence. Hydraulic losses and NO_X emissions are quantified to assess practical performance.

2. Experimental and diagnostic setup

This section describes the additively manufactured (AM) μ–slit injector and its structural characterisation, the custom-built single-nozzle piloted jet spray burner (PJSB) [40] together with its operating conditions, and the corresponding diagnostic setup.

2.1. Burner facility

A schematic of the developed atmospheric single-nozzle piloted jet spray burner (PJSB) is shown in Fig. 1. The burner provides well-defined, independently controllable boundary conditions for spray combustion studies over a wide range of operating conditions [50]. The origin of the coordinate system is defined at the centre of the combustor nozzle exit, with the axial direction aligned with the main airflow and the radial direction defined outward from the burner axis.

Upstream of the combustor nozzle, the main combustion air passes through a pre-conditioning plenum in which large-scale flow non-uniformities are attenuated by means of multiple flow deflections and a porous plate. The flow is subsequently accelerated through a contraction nozzle designed according to established wind-channel criteria in order to minimise separation and ensure a uniform exit profile [51]. The main combustor nozzle has an inner diameter of $D_c = 12$ mm and an outer diameter of 16 mm. The primary combustion air is regulated by a calibrated mass flow controller (Bronkhorst, In-Flow series, ±0.5%), enabling accurate control of jet velocity. Additionally, the air can be preheated up to 800 K (measured within the contraction nozzle exit) using a PID-controlled electric inline heater (Leister LE 10000 DF-R, ±0.7%).

The main assembly incorporates a centrally mounted liquid fuel injection system. Liquid fuel (Jet-A1) is introduced through three fuel inlet ports and conveyed via an internal fuel distribution channel (indicated in the yellow region, see Fig. 2). Section A–A in Fig. 1 provides a detailed cross-sectional view of the combustor nozzle assembly integrated with the annular AM μ-slit injector. In the conventional dual AB injector configuration, fuel is supplied via a centralised water-cooled lance, maintaining a temperature of 315 K (±0.5%) at the injector tip. Further details of the injector configuration are provided in previous work [40]. The liquid fuel is delivered from a nitrogen-pressurised reservoir, with the upstream pressure stabilised using a precision diaphragm regulator (Hornung, DH1 series) and fine-tuned via a pressure vent valve. The resulting liquid mass flow rate is monitored and regulated using a Coriolis-type mass flow controller (Bronkhorst, mini CORI-FLOW series, ±0.5%).

The co-annular pilot burner surrounds the main combustor nozzle, providing a continuous ignition source for stabilising the spray jet flame, under atmospheric open-configuration conditions. The pilot flame operates with a premixed gaseous blend of $80\%_{vol}$ H_2 / $20\%_{vol}$ CH_4 / air. Homogenisation of the mixture is achieved through a dedicated gas mixing and flow distribution unit, which simultaneously functions as a flashback arrestor [50]. The mixture is introduced into the pilot plenum and discharged circumferentially through tilted holes and AM porous media to form a stable annular flame. A shield-air sintered plate installed in the outer annular region protects the nozzle exit from ambient disturbances. Each pilot gas stream is independently regulated by calibrated mass flow controllers to allow precise adjustment of equivalence ratio and thermal load.

This modular PJSB configuration enables independent control of jet temperature and velocity, liquid fuel injection, and the enthalpy of the entrained hot gases, thereby providing a reproducible platform for systematic spray–flame investigations.

2.2. AM μ–slit injector and modified design parameters

A schematic of the developed novel AM μ–slit injector is presented in Fig. 2(a) and (b). The injector is fabricated using a laser-based powder bed fusion (PBF-LB/M) system (TruPrint 1000, TRUMPF) with a maximum laser power of 200 W and a laser spot diameter of 30 μm. Inconel 718 powder supplied by Carpenter Technology Corporation is utilised as feedstock material, featuring a particle size (d_p) distribution of $d_{p,10} = 24$ μm, $d_{p,50} = 36$ μm, and $d_{p,90} = 47$ μm [52]. The material is selected due to its high-temperature and oxidation resistance, making it suitable for combustion applications.

Liquid fuel is conveyed into the plenum and radially distributed into a co-annular fuel channel via three supply ports (see yellow region in Fig. 2). The fuel then passes through a gradually contracting channel into a 2 mm long ($l_{r,\mu\text{-}s}$) annular micro-slit, which promotes circumferential pressure equalisation prior to discharge at the nozzle exit. The measured slit width ($\overline{w_s}$), defined as the gap between the AB wall and the inner air-guiding wall at the exit, is 52 μm. This geometric accuracy is quantified by μ-XRCT analysis in Section 4.1. The vertical outer-wall region shows an areal surface roughness of approximately 23 μm. Following fuel discharge through the slit, a liquid film develops along the inner AB wall over a film length of $l_{wf} = 8$ mm before reaching the airblast edge. Inner and outer guiding vanes are incorporated to streamline the airflow and to ensure concentric alignment of the injector within the combustor nozzle. The outer vanes are positioned at $l_r = 10$ mm from the slit exit and extend over a length of $l_{ov} = 11$ mm, consistent with the AM airblast module design reported previously [40]. The inner vanes have a diameter of $D_{iv} = 5$ mm and are designed to replicate the geometric air split into coflow and atomisation air as in the dual prefilming AB injector configuration. Fig. 2(c) illustrates the implemented structural variations. The baseline configuration (S1) corresponds to the geometry shown in Fig. 2(a) and (b). Configuration S2 incorporates three μ-bumps on the AB wall, oriented perpendicular to the main flow direction, to enhance liquid-film disturbance along the wall surface. Configuration S3 integrates a low-swirl vane arrangement (vane inclination angle $\alpha_s = 30°$) to introduce controlled circumferential forcing and to modulate the coflow air velocity interacting with the liquid film. Detailed geometric parameters are summarised in Table 1.

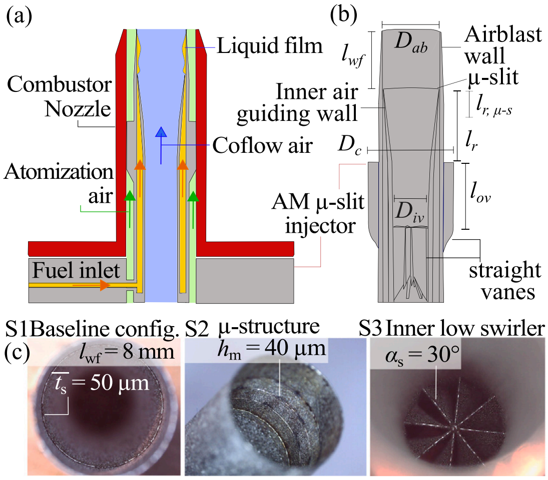

Fig. 2. Detailed flow schematic of the AM μ–slit injector (a) assembled with the combustor nozzle. Green and blue arrows indicate the atomisation air and the surrounding co-flow air interacting with the liquid film along the airblast wall, while the orange arrows denote the liquid fuel flow direction. The schematic (b) shows the detailed injector geometry together with the corresponding dimensional notations. The bottom images present the three investigated μ–slit injector configurations, characterised by a wall-film length of 8 mm (S1), the incorporation of μ-bumps (S2), and a low-swirl vane arrangement (S3). The dual AB configuration incorporating a pressure-swirl injector (C1) is detailed in previous work [34].

In total, four injector types are investigated to evaluate the feasibility of the μ–slit concept. Configurations S1–S3 use the μ–slit fuel discharge concept, whereas C1 utilises an in-house PS injector in an AB prefilming configuration [34,39–41].

2.3. Operation conditions

A wide operational range is investigated to examine the spray and combustion dynamics, accounting for both aerodynamic and fuel loading effects. The baseline condition is defined by an air jet bulk velocity (u_j) of 120 m/s, a liquid mass flow rate ($\dot{m}_l$) of 0.4 g/s, yielding an equivalence ratio (Φ) of 0.80, and an air preheating temperature (T_j) of 650 K for slit injectors, while $\dot{m}_l$ is set to 0.3 g/s for the C1 case (conventional AB concept). Variations in $\dot{m}_l$ range from 0.3 to 0.6 g/s (corresponding to $0.60 \leq \Phi \leq 1.2$) for the slit-injector family, while it ranges from 0.1 to 0.5 g/s ($0.20 \leq \Phi \leq 1.0$) for C1. The range of u_j is varied from 80 to 160 m/s. A summary is provided in Table 2 for the cases including detail spray analysis, while overall test conditions are provided in the Supplementary Material and Methods (SMM), Table S1.

Jet-A1 is used as liquid fuel, containing approximately 19% aromatic components as determined from fuel analysis. For the dual AB injector, the fuel temperature at the orifice exit is maintained at 315 K.

Table 1

Overall design parameters and representative operating conditions. “Slit” and “AB” denote the liquid fuel injection concepts, where the CAD-based slit width ($w_{s,c}$) is set to 50 μm, while the dual AB injector features an orifice diameter of 180 μm. The parameter l_{wf} refers to the wall-film length. The symbols α and H represent the structural inclination angle and height, respectively. Subscripts s and m indicate the inner swirler and the μ-bump structures, respectively.

Injector	S1	S2	S3	C1
Type	Slit	Slit	Slit	AB
$w_{s,c}$ [μm]	50	50	50	180
l_{wf} [mm]	8	8	8	8
α_s [°]	0	0	30	0
α_m [°]	0	90	0	0
h_m [μm]	0	40	0	0

In contrast, for the μ-slit injectors, direct measurement of the liquid temperature within the μ-slit is not feasible; therefore, the associated thermal effects are assessed indirectly, as discussed below. The pilot flame operates at an unburnt bulk velocity of 1.5 m/s with an equivalence ratio $\Phi = 0.65$, corresponding to an adiabatic flame temperature $T_{p,\mathrm{ad}}$ of approximately 1850 K and a thermal power of 15 kW. The pilot operating condition is kept constant throughout all measurements to maintain comparable flame stabilisation conditions, with anchoring governed by the entrainment of pilot-generated hot products into the main reaction zone. This enables relative comparison between injector configurations under identical stabilisation conditions. The actual pilot flame temperature, measured using a B-type thermocouple with radiation correction, is approximately 1470 K along the radial direction [50]. The outer shielding airflow is fixed at 60 g/s.

The non-dimensional numbers are evaluated using the measured d_{32} at $z = 0.5D_c$, determined from radial profiles between the centreline and the nozzle edge, directly downstream of the primary atomisation region. These parameters quantify the relative contributions of inertial, viscous, and surface tension forces governing droplet breakup. The jet Reynolds number Re_j is calculated using the combustor nozzle diameter D_c and the jet velocity u_j. The droplet Reynolds number Re_d is defined using the droplet diameter d and the axial droplet velocity $u_{z,d}$, whereas the slip Reynolds number Re_s is based on the slip velocity $u_{z,s}$ and the Sauter mean diameter d_{32}. Herein, $u_{z,s}$ denotes the axial slip velocity, defined as $u_{z,s} = |u_z - u_{z,d}|$, where u_z represents the gas-phase velocity and $u_{z,d}$ the instantaneous axial droplet velocity. The gas-phase velocity is estimated using tracer droplets with a diameter below $d_g = 5\,\mu\mathrm{m}$, selected to ensure sufficient responsiveness to the gas-phase flow [47]. Under the present conditions, the corresponding Stokes number (St) remains well below unity for all operating cases, confirming that d_g is appropriate for representing the gas-phase velocity. Further details on coincidence handling and velocity conditioning are provided in [47]. The slip Weber number We_s is formulated using the slip velocity and d_{32} to characterise the aerodynamic forcing acting on the droplets. The Ohnesorge number Oh relates viscous to surface tension effects based on d_{32}. In Eq. (1), ν and μ denote the kinematic and dynamic viscosity, while ρ and σ represent density and surface tension, respectively. The subscripts j and l refer to the gas and liquid-phases. All calculated non-dimensional numbers are summarised in Table 2 for the investigated operating conditions.

$$\begin{aligned} Re_j &= \frac{u_j \cdot D_c}{\nu_j} \;;\quad Re_d = \frac{\overline{u_{z,d}} \cdot d}{\nu_j} \;;\quad Re_s = \frac{\overline{u_{z,s}} \cdot d_{32}}{\nu_j} \;; \\ We_s &= \frac{\rho_j \cdot \overline{u_{z,s}}^2 \cdot d_{32}}{\sigma} \;;\quad Oh = \frac{\mu_l}{\sqrt{\rho_l \cdot \sigma \cdot d_{32}}} \end{aligned} \tag{1}$$

2.4. Diagnostic setup

In the present study, a μ-XRCT system is utilised to characterise the internal geometry of the AM injector. Spray characteristics are investigated using PDI and shadowgraphy, while OH* chemiluminescence (CL) imaging and exhaust gas sampling are used to assess the combustion process and performance. A schematic overview of the optical setup is provided in the SMM Fig. S1.

2.4.1. Micro X-ray computed tomography system (μ-XRCT)

The internal geometry of the AM μ-slit injector is characterised using a laboratory-scale μ-XRCT system. A micro-focus X-ray source (FineTec FORE 180.01C TT) is operated at 120 kV and 12 W, and projection images are recorded using a Shad-o-Box 6K HS flat-panel detector (2940 × 2304 pixels). The injector is mounted on a multi-axis motorised stage and scanned in cone-beam configuration with a source-object distance of 102 mm, yielding a geometric magnification of ≈9.9 and an isotropic voxel size, Δ_{vox} of 5.0 μm. Tomographic acquisition is performed over ±180° using 1800 projection angles with an exposure time of 3000 ms per projection. Detector non-uniformities are corrected using dark/open beam images and a calibrated pixel map, and a detector-shift strategy (±19 pixels in vertical and horizontal directions) is applied to suppress ring artefacts. The reconstructed volumes are obtained via filtered back-projection with geometric calibration, enabling quantitative resolution of the slit topology at micrometre scale. Additional details on the system configuration, operation, and calibration can be found in [53].

2.4.2. Phase Doppler interferometry (PDI)

A three-phase Doppler interferometry system (Artium Technologies Inc., Model PDI-300MD) is utilised to measure droplet size distributions and velocity components. The system incorporates diode-pumped solid-state lasers emitting at wavelengths of 532 nm (green), 491 nm (blue), and 561 nm (yellow). The transmission optics have a focal length of 350 mm with a beam separation of approximately 60 mm, resulting in nominal probe beam waists of 169, 156, and 179 μm in diameter for the respective laser pairs. The green laser pair is used to measure the axial velocity component and droplet diameter, while the blue and yellow laser pairs resolve the radial and circumferential velocity components, respectively. The PDI receiver operates in a 40° forward-scattering configuration. The receiver optics feature a fixed focal length of 350 mm and an aperture slit width of 100 μm. Under these settings, droplet diameters in the range of approximately 0.7–112 μm are measurable.

2.4.3. Shadowgraphy

Background-illuminated shadowgraphy is utilised to visualise spray formation. The second harmonic of an Nd:YAG laser (10 Hz repetition rate) is directed onto a white diffuser and a fluorescent plate, producing peak emission at 655 nm with a decay time of approximately 20 ns, thereby providing uniform pulsed back-illumination. Image acquisition is performed using a backside-illuminated CMOS camera (LaVision, CX12) equipped with a 180 mm Sigma macro lens operated at $f/2.8$. The field of view is approximately 10.3 × 14.4 mm^2 (2984 × 4080 pixel^2), corresponding to a spatial sampling of 3.5 μm / pixel and a measured optical resolution of approximately 7 μm, determined using a USAF 1951 resolution target (Thorlabs, R3L3S1N). A total of 500 images are recorded for each operating condition to ensure statistical convergence of the liquid injection behaviour.

Table 2

Overview of the reference test conditions for injectors S1–S3 and C1. The liquid mass flow rate $\dot{m}_l$, air jet bulk velocity u_j, preheated air temperature T_j, and equivalence ratio Φ are listed together with the air mass flow rate $\dot{m}_j$ and the air-to-liquid mass ratio (ALR). The non-dimensional parameters Re_d, Re_s, and We_s denote the droplet Reynolds number, gas-droplet slip-based Reynolds number, and Weber number, respectively, while Oh represents the Ohnesorge number. The Sauter mean diameter is given by d_{32}, and the thermal power is represented by P_{th}.

Injector	$\dot{m}_l$ [g/s]	u_j [m/s]	T_j [K]	Φ [–]	$\dot{m}_j$ [g/s]	ALR [–]	Re_j [–] $\times 10^4$	Re_d [–]	d_{32} [μm]	Re_s [–]	We_s [–] $\times 10^2$	Oh [–] $\times 10^2$	P_{th} [kW]
S1	0.30	120	650	0.60	7.37	24.6	24.6	10.1	10.8	0.44	0.58	8.61	12.9
	0.40	120	650	0.80	7.37	18.4	24.6	11.7	14.5	1.12	1.51	7.49	17.2
	0.50	120	650	1.00	7.37	14.7	24.6	13.4	17.8	2.02	3.00	6.81	21.5
	0.40	80	650	1.20	4.91	12.3	16.4	10.3	22.9	2.04	2.20	5.97	17.2
	0.40	160	650	0.60	9.83	24.6	32.8	13.0	12.2	0.21	0.18	8.35	17.2
S2	0.30	120	650	0.60	7.37	24.6	24.6	9.31	10.1	0.25	0.19	8.90	12.9
	0.40	120	650	0.80	7.37	18.4	24.6	10.7	14.1	0.83	0.78	7.66	17.2
S3	0.30	120	650	0.60	7.37	24.6	24.6	6.13	9.41	0.07	0.04	10.2	12.9
	0.40	120	650	0.80	7.37	18.4	24.6	9.05	10.9	1.06	1.99	9.08	17.2
C1	0.30	120	650	0.60	7.37	24.6	24.6	12.2	13.7	0.46	1.66	8.10	12.9

*2.4.4. OH**-chemiluminescence*

The combustion process is characterised via OH*-chemiluminescence (OH*-CL) imaging to assess flame lift-off height, flame penetration, and asymmetry metrics. For all configurations, an intensified relay optic (IRO) system equipped with a Halle UV quartz glass lens and a narrow band-pass filter (AHF, peak transmission 85%, 310 ± 15 nm) is used to isolate the OH* emission. Gain and gate time are maintained within 75%–80% and 10–12 μs, respectively. Background correction is performed using sensitivity images accounting for the adjusted gain and exposure time (see Section 3). For the μ-slit injector configurations (S1 – S3), quasi-steady OH*-CL imaging is conducted using a LaVision NanoStar IRO system. A total of 200 instantaneous images are recorded at 10 Hz. The field of view is 144.1 × 144.1 mm^2 (2048 × 2048 pixels), corresponding to a spatial sampling of 0.07 mm/pixel, with a measured optical resolution of approximately 0.25 mm. To capture the axially elongated flame structure, two image batches with an axial offset of 80 mm are acquired and subsequently stitched after background correction. The resulting expanded field of view is 144.2 × 224.1 mm^2, while preserving the optical resolution. For the reference configuration (C1), high-speed OH*-CL imaging is performed in a separate measurement campaign using a LaVision HighSpeed IRO X coupled with a Photron FastCam SA5 high-speed camera. A total of 10,000 instantaneous images are acquired at 10 kHz. The field of view spans 106 × 210 mm^2 (522 × 1031 pixels), corresponding to a spatial sampling of 0.20 mm/pixel, with a measured optical resolving power of approximately 0.63 mm. Despite differences in spatial and temporal resolution, identical spectral filtering and gain/gate settings ensured comparability of the OH* intensity fields across configurations.

2.4.5. Flame photographs

For a comprehensive analysis, direct flame images are captured using a DSLR camera (Canon, 500D). To ensure a consistent comparison of flame luminescence, the aperture, shutter speed, and ISO settings are maintained constant across all cases.

2.4.6. Exhaust gas analysis

The NO_X analysis involves sampling gases for a duration of 180 s once stable conditions are established, with data recorded at a frequency of 1 Hz. An air-cooled sampling probe, positioned 400 mm above the centre of the combustor nozzle exit, prevents further reactions by quenching the products. Detailed information regarding the measurement location sensitivity can be found in a previous study [40]. The collected gas is then conveyed through a heated hose to the gas analyser (MRU, MGAprime) to prevent water condensation during transport. A subsequent correction to 15% O_2 is applied to $X_{NO_X,c}$ for standardised comparison. Due to the open atmospheric flame configuration and the inevitable entrainment of pilot exhaust products, shield air, and ambient air, the reported NO_X levels are interpreted primarily in terms of relative injector-to-injector trends under otherwise identical operating conditions. Operation with the pilot flame and main airflow alone, i.e., in the absence of the main spray flame, resulted in NO_X levels below the detection limit, indicating that the reported emission trends are predominantly governed by the main liquid-fuel combustion process.

3. Methodology for statistical analysis

3.1. μ-XRCT-based structural characterisation

A slice-wise μ-XRCT workflow is used to quantify the circumferential uniformity of the annular slit channel. For each slice, the normalised intensity field is flattened to construct the intensity histogram, which exhibits a clear bimodal distribution corresponding to the wall and void phases. A robust void threshold is defined from the low-intensity population ($I_p \leq 0.5$) as the 99th percentile, providing a conservative upper bound of the void peak and excluding ambiguous boundary pixels at the wall–slit interface.

Following binary segmentation, the void field is restricted to the annular region using a geometrically defined mask to exclude neighbouring injector structures (e.g., vanes and outer walls). Conditional morphological closing operations are applied to regulate connectivity and suppress artefacts associated with wall pores. Connected-component labelling is used to retain only the dominant ring-like slit structure. The cleaned slit network is skeletonised to extract its geometric centreline. Local slit thickness is computed from the Euclidean distance transform of the retained void mask, evaluated along the centreline and converted using the μ-XRCT voxel size Δ_{vox}. The local thickness w_s is defined as twice the distance-transform value at each centreline coordinate and is evaluated along the cleaned slit network, as shown in Fig. 3(a).

Sensitivity of the extracted slit-width statistics over $z_s = -0.5$ to 0 mm is assessed with respect to the morphological kernel size, percentile threshold, and number of skeleton branches. The results exhibit limited dependence on these parameters, with variations of approximately ±6% in $\overline{w_s}$ for kernel sizes between 3–7 pixels and less than 5% variation in the angle fraction of blocked segments ($\Delta\theta_{bs} = N_{bs}/N_\theta \times 2\pi$). Threshold variation (98.5–99.5%) for low-intensity range results in changes below ±3.5% in $\overline{w_s}$, while skeleton-branch variation produces less than 1.5% deviation, confirming overall robustness. Thin regions are defined by the physical criterion $w_s < w_{thr}$, where $w_{thr} = 15\,\mu m$ corresponds to the lower bound of the feedstock powder particle size distribution. This choice is supported by a sensitivity analysis, showing negligible variation (< 0.5%) for $w_{thr} = 10 - 15\,\mu m$, while larger thresholds introduce deviations of up to 2% in $\Delta\theta_{bs}$. Circumferentially blocked regions are identified from discontinuities (red marks) in the slit centreline, as shown in Fig. 3(b). A reference circle is fitted to the extracted centreline, and the angular positions of the skeleton points

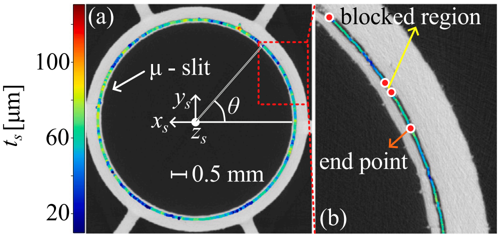

Fig. 3. Horizontally sliced μ-XRCT image (a) with a magnified view of the scaled-down μ-slit injector, highlighting the blocked region (b_s), skeleton endpoints, and the local slit gap width (w_s). The associated coordinate system (x_s, y_s, z_s) and the circumferential angle (θ) are indicated.

are computed directly from their pixel coordinates with respect to the fitted centre. Gaps between consecutive angular positions are then evaluated, and discontinuities are classified as blocked regions.

The circumferential dispersion of thin ($w_{s,15}$) and blocked regions (b_s) is quantified using the normalised angular entropy defined in Eq. (2):

$$H_N = \frac{-\sum_{i=1}^{N_\theta} p_i \ln p_i}{\ln N_\theta} \tag{2}$$

where $p_i = n_i / \sum_{j=1}^{N_\theta} n_j$ denotes the probability associated with the ith angular bin at axial position z_s, and n_i is obtained from the combined angular event set of $\theta_{w_{s,15}}$ and θ_{bs}. Here, z_s denotes the axial distance from the slit exit. The angular domain is discretised into uniform 1° bins for statistical aggregation, such that $N_\theta = 360$ in the present study. A relative occupancy filter (25% of the maximum bin count within each slice) is applied prior to entropy evaluation to suppress isolated angular events.

3.2. Phase Doppler interferometry

3.2.1. Statistical characterisation of droplet, velocity, and fuel-loading

The droplet PDI signals are processed to obtain droplet diameter, velocity, and droplet inter-arrival time (Δt_a). From these raw measurements (χ), the mean ($\overline{\chi}$) and standard deviation (χ') are evaluated as defined in Eq. (3). To ensure statistical robustness, datasets containing fewer than 1000 valid samples, or cluster samples below the lower outlier threshold of the total droplet measurements, are excluded to minimise the influence of rare measurement artefacts. Probe volume correction (PVC) is applied to address the bias that larger droplets are detected over a larger volume compared to smaller ones, due to the Gaussian intensity distribution of the laser beams. The Sauter mean diameter ($d_{32} = \Sigma d^3/\Sigma d^2$) is calculated by incorporating the PVC correction. For the analysis of turbulence–droplet interaction, the three components of the estimated gas-phase velocity (u_z, u_y, u_x), the turbulent kinetic energy ($k = (\overline{u_z'^2} + \overline{u_y'^2} + \overline{u_x'^2})/2$), and the axial slip velocity ($u_{z,s}$) are evaluated.

$$\overline{\chi} = \frac{1}{N}\sum_{n=1}^{N} \chi_n; \qquad \chi' = \sqrt{\frac{1}{N}\sum_{n=1}^{N} (\chi_n - \overline{\chi})^2} \tag{3}$$

To assess the radial homogeneity of the AM μ-slit injector in terms of the droplet diameter (d) and the local fuel loading ($\dot{m}_{f,lc}$), the first-order Wasserstein distance (D_{w1}) is evaluated between symmetric radial locations using Eq. (4). For each radial pair ($R = \pm 2, \pm 4, \pm 6, \pm 8$ mm), D_{w1} is calculated from the cumulative distribution functions (CDFs) F_l and F_r, on the left and right sides, respectively, constructed from the measured droplet samples at each radial location. Here, χ denotes either d, $\dot{m}_{f,lc}$, or the radial intensity I of OH*-CL. The local fuel feeding rate $\dot{m}_{f,lc}$ is evaluated from the droplet samples using Eq. (5) to assess the radial distribution and symmetry of fuel placement.

$$D_{w1} = \int_0^\infty \left| F_l(\chi) - F_r(\chi) \right| \, d\chi \tag{4}$$

$$\dot{m}_{f,lc} = \frac{\pi}{6} \frac{\rho_l d^3}{\Delta t_a} \tag{5}$$

When valid samples are available only on one side, the CDF on the opposite side is taken as a zero distribution, i.e. $F(\chi) = 0$, representing the absence of the fuel loading at that radial location. This definition yields a D_{w1} corresponding to the entire measured distribution and the pair is included in the radial averaging. A value of $D_{w1} = 0$ indicates perfectly identical distributions at symmetric radial locations, i.e., complete radial homogeneity within the pair.

3.2.2. Local group combustion using Voronoi-resolved droplet clustering

The cluster-resolved group combustion number is evaluated to quantify the influence of droplet clustering on flame stabilisation across different injection configurations and various radial positions. The analysis is based on time-resolved droplet detection signals obtained from PDI, where the droplet arrival time series t_a, instantaneous droplet velocities u_d, and droplet diameters d are processed using coincident samples. The temporal droplet sequence is first converted into a one-dimensional spatial representation of the spray by reconstructing the droplet positions along the measurement direction. The instantaneous inter-droplet spacing is estimated as $L_i = \Delta t_a u_{z,d}$, where $\Delta t_a = t_{a+1} - t_a$ is the inter-arrival time and $u_{z,d}$ is the axial droplet velocity. The cumulative summation of L_i yields the reconstructed spatial coordinate s, representing the one-dimensional droplet distribution.

In conventional group combustion analyses, droplet clusters are typically identified using a Δt_a threshold criterion, where droplet pairs are considered clustered when Δt_a is smaller than the convective time required for a droplet structure to traverse the probe height. In the present dataset, however, this criterion identified less than 3% of droplets as clustered events for all injector cases, reflecting the sparse droplet field caused by rapid evaporation and dilution, and limiting the statistical representativeness of cluster-resolved quantities. Therefore, the mean G_c values are reported in SMM Fig. S2 only as reference indicators of the prevailing droplet combustion regime.

Droplet clustering is therefore identified using a Voronoi tessellation applied to the reconstructed spatial distribution, providing a density-based measure of local droplet concentration that remains applicable even for evaporating sprays with low droplet number density [54]. The local Voronoi segment length is defined as $V_i = (s_{i+1} - s_{i-1})/2$, representing the local spacing surrounding each droplet i [55]. The Voronoi lengths are normalised by their mean value, $\overline{V}$. Droplets are classified as belonging to a cluster when $V_i < 0.5\overline{V}$, corresponding to Voronoi cells smaller than those expected for a random particle distribution and therefore indicating locally enhanced droplet concentration relative to a random distribution. The characteristic cluster length scale is then estimated from the spatial extent of the detected cluster as $L_c = s_{i_{\max}+1} - s_{i_{\min}} - L_p$, where $i_{\min}$ and $i_{\max}$ denote the first and last droplet indices belonging to each cluster, respectively. Here, L_p is the probe length scale, defined as $(L_{p,x} L_{p,y} L_{p,z})^{1/3}$, where $L_{p,x}$, $L_{p,y}$, and $L_{p,z}$ denote the aperture size, width, and height of the probe beam, respectively.

The cluster number density is evaluated as $n_T = (\pi/6)(L_c/L)^3$, where L denotes the mean inter-droplet spacing, L_i. The non-dimensional droplet separation between droplet centres is defined in Eq. (6), where d_{10} is the arithmetic mean droplet diameter and Re_d is the droplet Reynolds number. Finally, the cluster-resolved group combustion number is calculated as defined in Eq. (7), following the classical group combustion formulation proposed by Chiu et al. [56] and its experimental extensions to spray flames [57]. For kerosene vapour–air mixtures, a Lewis number of $Le = 4$ and Schmidt number of $Sc = 3$ are used as conservative estimates for the present cluster-resolved scaling analysis [58].

$$S = \frac{L/10d_{10}}{1 + 0.276\, Sc^{1/3} Re_d^{1/2}} \tag{6}$$

$$G_v = 0.15\, Le \frac{n_T^{2/3}}{S} \tag{7}$$

According to group combustion theory [56], the burning mode of a droplet cluster is governed by the group combustion number G. For $G < 1$, oxidiser penetration into the cluster core is sustained and combustion proceeds in an internal group combustion mode, whereas $G > 1$ promotes external sheath burning characterised by vapour shielding and the formation of a surrounding diffusion envelope. The present spray flame is not interpreted as a fully developed group combustion regime. Instead, the relative variations in G_v are used to quantify injector-dependent changes in collective droplet interaction, local vapour enrichment, and the tendency towards isolated or collective evaporation behaviour, which in turn influence flame anchoring and lift-off sensitivity.

*3.3. OH**-*chemiluminescence*

For robust OH*–CL image analysis, a background-correction and preprocessing algorithm is applied [34,47]. A case-dependent background field is first obtained from the temporal minimum of a subset of instantaneous images and subsequently smoothed to remove local artefacts. After excluding outliers, an adaptive global threshold is defined from an upper quantile of the background intensity distribution, complemented by its standard deviation and scaled by tunable coefficients (c_1, c_2). Each instantaneous image is filtered using a two-dimensional moving average filter with kernel width f_w to suppress high-frequency noise, and is then thresholded according to the defined criterion. The resulting binary field is further refined by hole filling to obtain a consistent flame mask.

For elucidating the combustion process corresponding to each injector concept, the flame lift-off height (l_{loh}), maximum intensity axial location (l_{max}), and axisymmetry metrics, including the deviation of l_{loh} (Δl_{loh}), area asymmetry (A_{asym}), normalised cross-correlation (ψ), and the Wasserstein distance of OH*–CL intensity ($D_{w1,I}$) between the left and right sides of the frame, are evaluated. These metrics are subsequently averaged, and their standard deviations are calculated across all image sets using Eq. (3). The definitions of A_{asym} and ψ are given in Eqs. (8) and (9), respectively, while $D_{w1,I}$ is computed according to Eq. (4). The l_{loh} is defined as the axial location of the earliest binary transition. l_{max} denotes the axial location of maximum OH* intensity. The flame penetration length is not calculated due to limitations of the measurement frame area.

Here, A_l and A_r denote the flame areas extracted from the binarised OH* mask on the left and right halves of the image, respectively. The normalised cross-correlation coefficient ψ is evaluated from OH* intensity fields $I'_{OH*,l}(x,z)$ and $I'_{OH*,r}(x,z)$, where (x,z) represent the spatial coordinates and (i,j) denote the relative axial and radial pixel shift used to determine the maximum correlation. The Wasserstein distance $D_{w1,I}$ corresponds to the first-order transport distance between the left and right OH* intensity distributions, quantifying the degree of distributional intensity asymmetry beyond purely geometric differences. By definition, $A_{\mathrm{asym}} = 0$ and $D_{w1,I} = 0$, and $\psi = 1$, correspond to perfect symmetry between the two sides of the flame, whereas larger values of A_{asym} and $D_{w1,I}$ or lower values of ψ indicate increasing asymmetry.

$$A_{\mathrm{asym}} = \frac{|A_l - A_r|}{A_l + A_r} \tag{8}$$

$$\psi = \frac{\max_{i,j}\left(\sum_{x,z} I'_{OH*,l}(x,z) \cdot I'_{OH*,r}(x+i, z+j)\right)}{\sqrt{\left[\sum_{x,z} I'^2_{OH*,l}(x,z)\right] \cdot \left[\sum_{x,z} I'^2_{OH*,r}(x,z)\right]}} \tag{9}$$

The influence of the filtering window width and threshold coefficients on the extracted flame metrics is evaluated through a dedicated sensitivity analysis (see Table S2 in the SMM). The moving-average filter width (f_w) is varied to values corresponding to the minimum integral length scale of the flow [47], accounting for differences in pixel resolution between the μ-slit and AB datasets. The threshold coefficients (c_1, c_2) are perturbed by approximately ±10% from the baseline value (2.5). Across all perturbations, the majority of extracted metrics exhibit deviations below 10% relative to the baseline. Larger percentage variations, approaching 20%, are observed primarily for l_{loh} in the AB configuration, which reflects its smaller baseline magnitude and inherently larger fluctuation levels rather than numerical instability. In contrast, the peak intensity location l_{max} exhibits only marginal variation (< 1%), indicating high robustness of the core flame-structure identification. Furthermore, the applied perturbations do not modify the qualitative trends or comparative relationships discussed in the main text, supporting the overall consistency of the adopted image-processing framework.

4. Results and discussion

4.1. AM μ-slit structural topology

The fabrication of narrow annular slits by PBF-LB/M is inherently accompanied by stochastic geometric deviations, including percolating pore networks, incomplete fusion between adjacent scan tracks, melt-track balling, and partially fused powder agglomeration, which may locally constrict the flow channel or alter the effective gap width [16,50,59]. The μ-XRCT analysis provides a quantitative assessment of both the geometric accuracy and the circumferential uniformity of the AM annular channel. For this purpose, reduced-scale specimens corresponding to the injector head geometry are fabricated, allowing μ-XRCT measurements of the slit structure. The specimen features a continuously decreasing nominal slit gap from 110 μm to 50 μm, enabling identification of the minimum manufacturable gap achievable with the current PBF-LB/M process. The methodology for the statistical analysis of the μ-XRCT images is described in Section 3.1. It should be noted that the present analysis is based on two injector specimens, and piece-to-piece geometric variations are expected due to manufacturing tolerances. Nevertheless, the stochastic nature of the local blockage redistribution may contribute to a more circumferentially balanced discharge behaviour.

Fig. 4(a) compares the measured local slit gap (w_s) with the nominal CAD geometry along the axial coordinate. While the overall trend obtained using piecewise linear fitting follows the CAD-designed tapering profile, systematic deviations are observed towards the slit exit. The region of $-0.2 \le z_s$ (mm) ≤ 0.0 is omitted because the wall geometry becomes progressively one-sided and discontinuous. In particular, a plateau region with an average gap width of 52 μm and a standard deviation of 17.2 μm develops near $z_s \approx -0.6$ mm, indicating a process-induced limitation in achieving the intended minimum printable gap. This behaviour suggests that the effective manufacturable resolution of the PBF-LB/M process approaches the lower bound of the nominal design in this region. Fig. S3 in the SMM further compares the axial evolution of the w_s between two independently manufactured AM μ-slit samples. Despite local variations, both samples exhibit comparable geometric trends with a mean w_s discrepancy of 4.10%, indicating good manufacturing reproducibility near the slit exit region. The axial variation of the circumferentially resolved thin and blocked regions is shown in Fig. 4(b). Thin segments ($w_s < 15$ μm) and blocked angular portions exhibit increasing occurrence density towards the slit exit, revealing enhanced circumferential delocalisation of thin and blocked regions. While this behaviour reflects increasing geometric irregularity, the local bridging structures become progressively less biased towards specific angular sectors. Consequently, the downstream region approaches a statistically isotropic hydraulic resistance field.

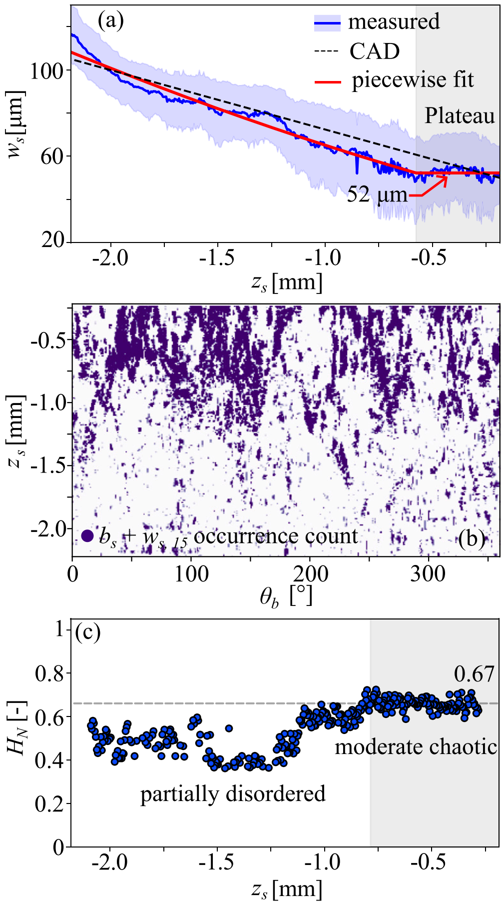

Fig. 4. Measured local slit gap (w_s) compared with the nominal CAD geometry along the axial coordinate (z_s) (a). The solid blue line denotes the mean w_s at each z_s, while the red piecewise fit highlights a saturation behaviour with a plateau at 52 µm. Panel (b) shows the circumferential distribution of thin and blocked angular segments (θ_b) as a function of z_s. Panel (c) presents the normalised angular entropy H_N versus z_s.

To quantify the evolution of circumferential delocalisation, the normalised angular entropy H_N is evaluated as a function of axial position (Fig. 4(c)). Upstream of the slit exit, H_N varies between 0.39 and 0.60, indicating partially disordered angular patterns with weak but discernible sectoral bias. In this region, geometric irregularities remain spatially correlated, favouring preferential fuel pathways along specific angular sectors. From z_s = -0.55 mm towards the slit exit, H_N increases to approximately 0.67, reflecting a broader redistribution of thin and blocked segments across the circumferential domain. Rather than representing purely chaotic behaviour, this entropy increase signifies a progressive reduction of dominant sectoral asymmetries and a transition towards a statistically isotropic circumferential topology. As a consequence, persistent preferential fuel flow is mitigated, and the hydraulic resistance field becomes more evenly distributed around the annulus, promoting balanced circumferential fuel discharge in the near-exit region.

4.2. Spray characterisation

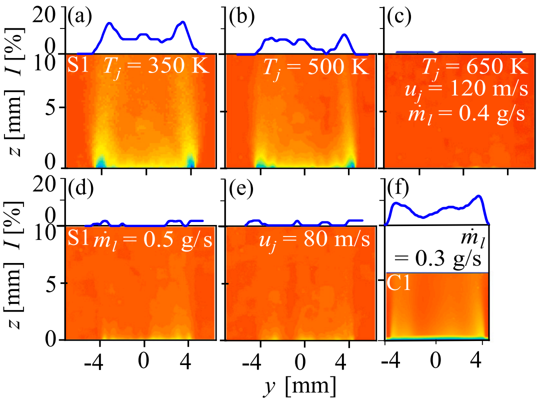

Fig. 5. Normalised average shadowgraphy images for S1 in panels (a-e) and C1 in panel (f) under various test conditions. Baseline operational conditions are shown in (c), while altered values are labelled in each image. Profile plots at the top of each image represent intensity profiles along the y-direction at $z/D_c = 0.25$.

The intensity-normalised average shadowgraphy images for the two injector concepts, S1 and C1, are presented in Fig. 5. Panels (a–e) correspond to S1 under varying operating conditions, while panel (f) shows C1 at its reference conventional case. The profile plots above each image depict the lateral intensity distribution along the y-direction at $z/D_c = 0.25$, providing a qualitative representation of the near-nozzle spray structure and relative fuel placement. Under the low T_j condition (a), the S1 injector exhibits a radially symmetric intensity distribution with peak values of 10% located at $y = \pm 3$ mm. This symmetric fuel placement reflects a uniform circumferential liquid sheet formation, directly linked to the stochastic gap connectivity, which promotes balanced circumferential fuel discharge at the slit exit. Meanwhile, the C1 injector (f) displays comparable peak intensity and reduced radial symmetry, with maxima located further from the centreline ($y \approx \pm 4$ mm). The latter arises from the PS injector, which directs liquid fuel towards the airblast wall with circumferential forcing. The influence of operating conditions is evident in panels (a–c). Increasing the co-flow temperature T_j from 350 K to 650 K results in a substantial attenuation of the shadowgraphy signal, indicating enhanced heat transfer from the preheated co- and atomisation air to the liquid film and partial pre-vaporisation of Jet-A1 within the µ-channel. The associated phase transition modifies both the effective fuel placement and the injector pressure drop characteristics, as further discussed in Section 4.4. Similarly, negligible signal intensity persists under increased liquid mass flow rate $\dot{m}_l$ (d) and reduced jet velocity u_j (e).

These qualitative observations highlight the near-field gas-phase turbulence and spray topology for the µ-slit and conventional injection concepts. To further elucidate the underlying mechanisms governing fuel dispersion and mixing, the turbulence–droplet interaction is examined in the following section.

4.2.1. Flow-field turbulence and droplet interaction

Radial profiles of the three droplet velocity components ($\bar{u}_{z,d}$, $\bar{u}_{x,d}$, $\bar{u}_{y,d}$; axial, radial, and circumferential) are presented at two axial positions of $z/D_c = 0.5$ and 2 with a fixed jet temperature of 650 K for different operating conditions in the left two columns of Fig. 6, and for various injector concepts in the right column. Symbols denote mean values for each case, and error bars indicate the corresponding fluctuations. Increasing the liquid mass flow rate ($\dot{m}_l$) from 0.3 g/s to 0.5 g/s for the S1 configuration, as shown in Fig. 6 (a – c), results in a concave $\bar{u}_{z,d}$ profile with only marginal variations. For the baseline condition ($\dot{m}_l = 0.3$ g/s), a maximum $\bar{u}_{z,d}$ of 131 m/s with $u'_{z,d} = 25$ m/s is observed at the radial edge ($x = \pm 5$ mm) at $z/D_c = 2$, decreasing to 81 m/s with $u'_{z,d} = 11$ m/s in the nozzle centre ($|x| \leq 2$ mm). Increasing $\dot{m}_l$ alters $\bar{u}_{z,d}$ by less than 5% at the radial edge and by less than 2% in the jet centre, suggesting a limited influence of liquid loading on the velocity field. The corresponding gas-phase velocity trends are shown in the SMM Fig. S4. The $\bar{u}_{x,d}$ component remains weak, with mean values of approximately ±12 m/s and fluctuations of about 2 m/s at $x = \pm 5$ mm,

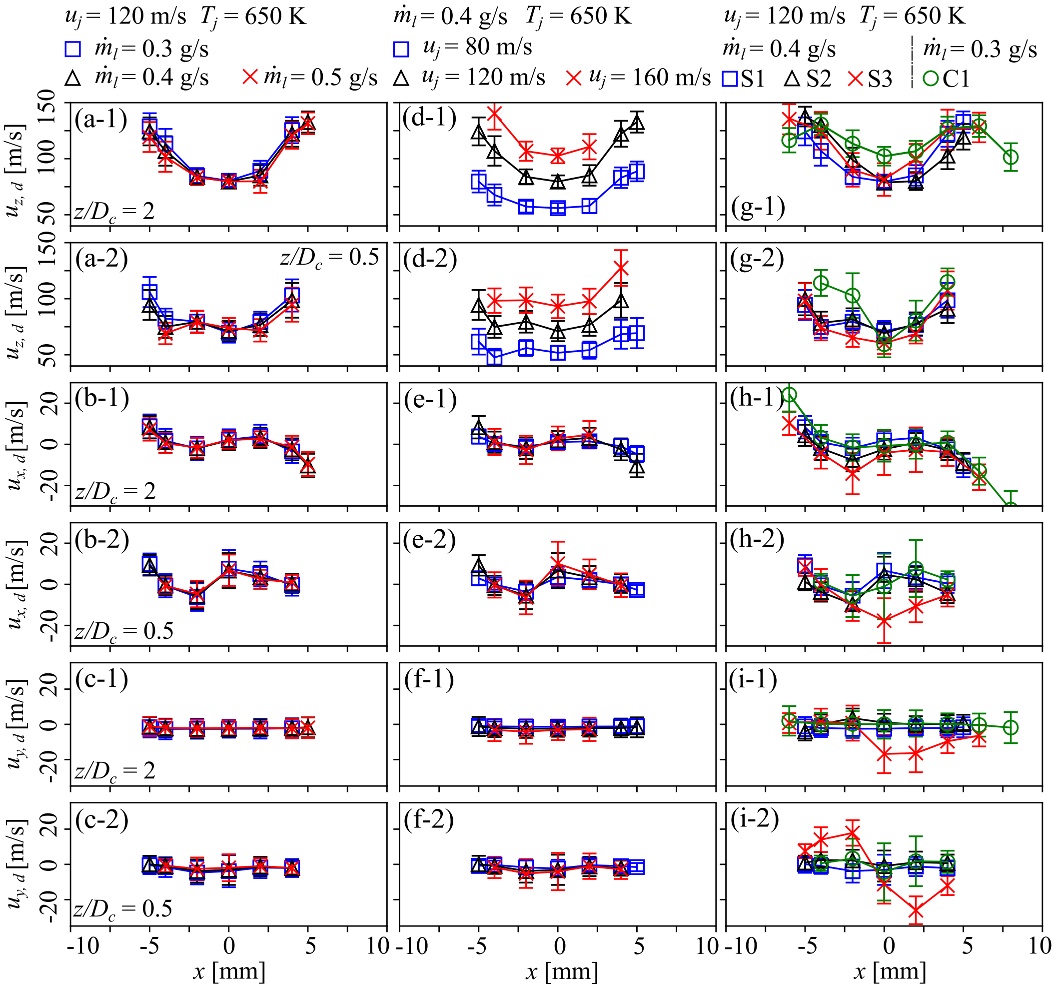

Fig. 6. Three-dimensional droplet velocity components, axial $u_{z,d}$, radial $u_{x,d}$, and circumferential $u_{y,d}$, measured at two axial positions; $z/D_c = 0.5$ (panel set 1) and $z/D_c = 2$ (panel set 2). Columns group operating conditions as follows: liquid loading effects, $\dot{m}_l$, (panels a–c), aerodynamic effects with varying jet velocity, u_j, (panels d–f), and injector variations (panels g–i). Symbols denote mean values of each component; bars indicate the corresponding turbulent fluctuations.

while the peak radial motion is located in the mixing layer due to the strong velocity gradient and associated entrainment. The centreline remains close to zero in agreement with previous observations [60]. The influence of aerodynamic forcing, achieved by varying the jet velocity (u_j) from 80 to 160 m/s as illustrated in Fig. 6 (d – f), leads to a pronounced increase in $\bar{u}_{z,d}$ and u'_z over the entire radial range. At $z/D_c = 2$, the centreline $\bar{u}_{z,d}$ increases from 58.6 to 107 m/s with $u'_{z,d}$ rising from 10 to 20 m/s, while at $x = 4$ mm, $\bar{u}_{z,d}$ increases from 68 to 142 m/s with u'_z from 20 to 30 m/s. In contrast, $\bar{u}_{x,d}$ and $\bar{u}_{y,d}$ remain nearly unchanged. The higher axial momentum enhances turbulence production and exhaust-gas entrainment, intensifying mixing with the surrounding hot gases, which likely promotes droplet evaporation and contributes to the observed 20% reduction in radial droplet extent.

Fig. 6(g–i) compares the droplet velocity fields produced by the different injector concepts. In the near field at $z/D_c = 0.5$, the conventional AB injector C1 exhibits comparable centreline values of $\bar{u}_{z,d} = 59$ m/s and $u'_{z,d} = 24$ m/s, but shows a radial droplet velocity deviation of about 20 m/s at $x = \pm 2$ mm, yielding elevated $u'_{z,d}$ up to 38 m/s and indicating coherent asymmetric structures in the near field [46–48]. This asymmetry is reduced to below 8 m/s further downstream at $z/D_c = 2$. The centreline $\bar{u}_{z,d}$ becomes approximately 20 m/s higher than in the S1 case and more radially uniform within $|x| \le 5$ mm, accompanied by a 17% wider droplet-laden region even at the lower fuel loading of 0.3 g/s. The structural modifications (μ-bumps, S2) and the low-swirler (S3) produce only minor changes in $\bar{u}_{z,d}$ relative to S1, yet S3 extends the droplet-laden region by about 20% at $z/D_c = 2$. While the effect on $\bar{u}_{x,d}$ remains small, the circumferential forcing in S3 and C1 enhances the velocity fluctuations, reaching 22 m/s and 31 m/s at the centre and about 15 m/s and 22 m/s within $|x| \le 2$ mm at $z/D_c = 2$. Notably, S3 exhibits a negative $\bar{u}_{x,d}$ of approximately -17 m/s near the nozzle centre in the upstream plane, consistent with the swirl-induced inward radial transport reported previously [40,47]. The co-flow swirl in S3 generates an enhanced $\bar{u}_{y,d}$, with a mean value of 22 m/s and fluctuations of 16 m/s at $x = \pm 2$ mm. In contrast, S2 and C1 show comparable mean $\bar{u}_{y,d}$ values close to zero, although C1 produces elevated $u'_{y,d}$ up to 27 m/s over $|x| \le 4$ mm. Further downstream, the circumferential droplet velocity components remain close to zero, with similar magnitudes observed for all cases except S3.

The measured gas-phase velocity, shown in the SMM Fig. S4, remains comparable in magnitude and trend to the droplet velocity, while the measurable region is limited by the number of coincident droplet samples. The swirl-induced motion of S3 is more evident in the gas-phase field. The modified gas-phase turbulence and its coupling with droplets are further assessed using the turbulent kinetic energy and axial slip velocity in the SMM Figs. S5 and S6. Overall, k is mainly governed by aerodynamic shear rather than liquid loading, with increasing u_j enhancing turbulence across the radial range. The C1 injector produces a more radially non-uniform turbulence field and broader slip-velocity distribution, indicating stronger phase-relative transport in the nozzle near field. In contrast, the μ-slit configurations

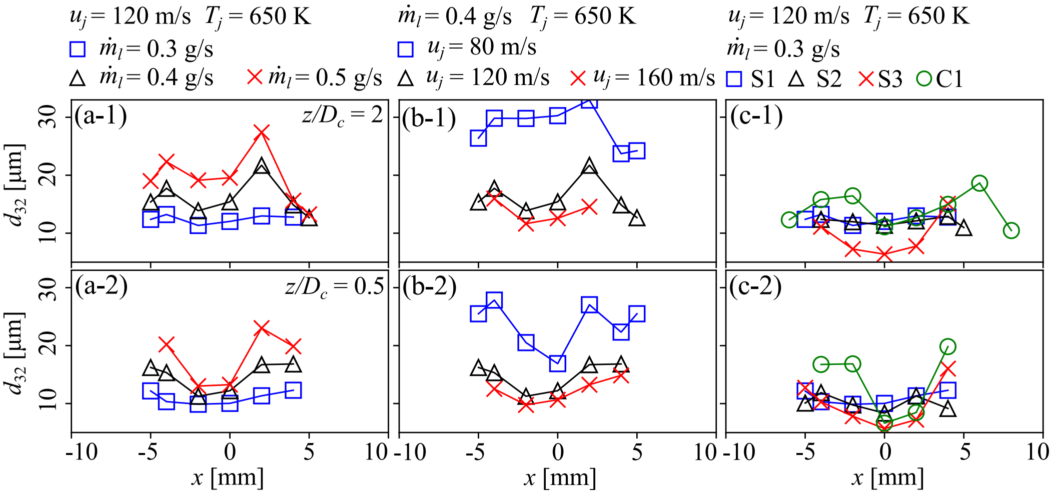

Fig. 7. d_{32} as a function of the radial coordinate, shown at two axial locations $z/D_c = 0.5$ and 2 (lower and upper rows, respectively). The first column (a–1 and a–2) presents fuel mass flow effects, and the second column (b–1, b–2) shows jet aerodynamic effects. The third column (c–1 and c–2) depicts injector variations at $\dot{m}_l = 0.3$ g/s.

maintain more constrained slip-velocity distributions, while the S3 configuration redistributes turbulence towards the jet core and promotes smaller droplets downstream through circumferential forcing.

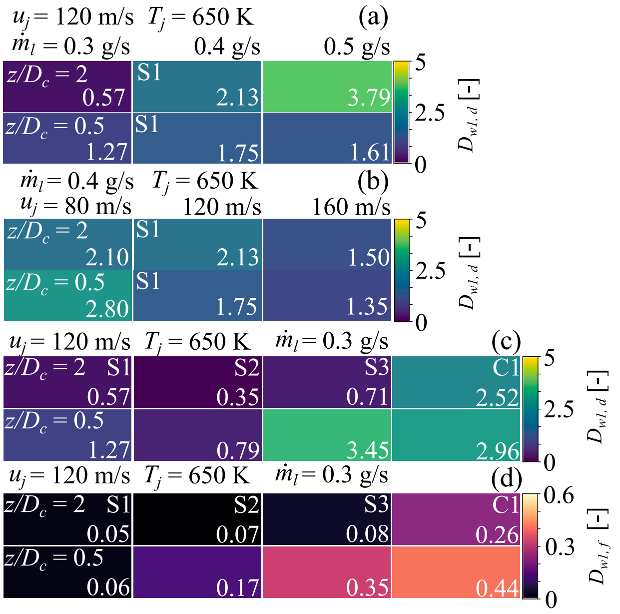

Fig. 8. Heat maps of the averaged Wasserstein distance ($\overline{D}_{W1}$), used as a measure of the radial dissimilarity of the cumulative droplet-size distribution (a–c) and the local fuel feeding rate (d). Panels are organised by operating condition and injector concept: mass flow rate variation (a), jet velocity variation (b), and comparison of the developed slit injectors S1–S3 with the conventional AB injector C1 (c, d). Within each group, the upper and lower rows correspond to $z/D_c = 2$ and 0.5, respectively.

4.2.2. Radial spatial spray distribution and uniformity

Atomisation performance is evaluated in terms of d_{32} along the radial direction for different operating conditions in Fig. 7(a, b) and injector concepts in Fig. 7(c). For the S1 configuration, increasing $\dot{m}_l$ from 0.3 to 0.5 g/s leads to a systematic increase in d_{32} over the entire radial range at both axial locations, with the peak value rising from 12.8 μm to 24.8 μm at $z/D_c = 2$ and from 14.8 μm to 24.3 μm at $z/D_c = 0.5$. Meanwhile, varying u_j strongly affects d_{32}, where the reduction in aerodynamic forcing at $u_j = 80$ m/s results in larger droplets with d_{32} up to 34.7 μm at $z/D_c = 2$, while further increasing u_j yields only marginal changes with an average size discrepancy of 0.3 μm across the radial direction, confirming the previously identified saturation of atomisation at high gas–liquid relative acceleration. For the injector concepts, the C1 configuration exhibits larger radial variations in d_{32} in the near field, ranging from 7.02 to 20.3 μm at $z/D_c = 0.5$, reflecting the broader droplet dispersion and stronger gas–liquid coupling. Notably, the droplet size discrepancy between the paired radial locations at $x = \pm 2$ mm reaches 8.39 μm, indicating pronounced radial inhomogeneity. In contrast, the μ-slit injectors (S1 and S2) show comparatively uniform d_{32} distributions with an average of 9.76 μm in the near field. Downstream, the swirl-induced transport in S3 promotes smaller droplets, with d_{32} reduced to a minimum of 6.57 μm at the nozzle centre at $z/D_c = 2$, consistent with the enhanced droplet–turbulence interaction observed in the slip-velocity statistics. Note that elevated liquid loading and aerodynamic forcing both magnify the radial inhomogeneity of droplet size in μ-slit injectors. Meanwhile, the C1 configuration produces the largest radial bias, directly coupled with the turbulence structure and fluctuation field.

The fuel spatial placement and the associated size distribution govern the local mixture stratification, which subsequently determines the flame axisymmetry and emission characteristics. Therefore, the radial similarity of the spray across the nozzle serves as an important metric. To quantify this spatial uniformity, the averaged Wasserstein distance, $\overline{D}_{w1,d}$, is evaluated as a measure of the dissimilarity of radial paired cumulative droplet-size distributions, as shown in Fig. 8. In panels (a), for the S1 configuration, increasing the liquid mass flow rate leads to a pronounced increase in $\overline{D}_{w1,d}$ at both axial locations, with values rising from 1.27 to 1.61 at $z/D_c = 0.5$, and from 0.52 to 3.79 at the downstream location $z/D_c = 2$, indicating enhanced radial dissimilarity under elevated liquid-phase momentum. In contrast, variation of the jet velocity shows a different behaviour in panels (b). At $u_j = 80$ m/s, $\overline{D}_{w1,d}$ reaches the highest level of approximately 2.80 at $z/D_c = 0.5$ and remains at 2.10 downstream, indicating strong radial inhomogeneity under aerodynamically limited atomisation. Increasing u_j to 120 and 160 m/s reduces $\overline{D}_{w1,d}$ to below 1.50 at both axial locations, confirming that stronger gas–liquid relative acceleration promotes a more homogeneous droplet field. Among the injector concepts shown in panels (c), the conventional C1 configuration exhibits a high radial inhomogeneity, with $\overline{D}_{w1,d}$ of 2.96 in the near field and remaining above 2.50 at $z/D_c = 2$, consistent with the previously identified asymmetric turbulent coherent structure and large radial droplet-size difference. In contrast, the introduction of the μ-slit fuel injection (S1) reduces $\overline{D}_{w1,d}$ by 57% and 77% at $z/D_c = 0.5$ and 2, indicating a substantially improved radial homogeneity of the droplet field. The μ-bump-integrated configuration (S2) produces a further mitigation of radial dissimilarity at both axial locations. Meanwhile, the low-swirler configuration (S3) increases $\overline{D}_{w1,d}$ upstream to 3.45 but rapidly relaxes it downstream to 0.71.

A similar trend is observed for the local fuel feeding rate metric shown in panels (d), where the slit injectors maintain $\overline{D}_{w1,f}$ below 0.10 downstream, corresponding to a reduction of more than 75% compared to the C1 configuration. This pronounced asymmetry of the droplet size (d) and local fuel feeding rate ($\dot{m}_{f,lc}$) in the radial direction for the different operating conditions and injector types is further illustrated in the SMM Figs. S7 and S8. These results quantitatively demonstrate that both elevated liquid loading and insufficient aerodynamic forcing magnify radial droplet non-uniformity, whereas the slit injector concepts promote homogenisation of the spray field. The improved radial homogeneity is consistent with the circumferentially balanced fuel discharge imposed by the AM μ-slit topology (see Section 4.1). The increase in the stochastic gap connectivity suppresses dominant sectional bias and promotes a statistically isotropic circumferential flow distribution at the slit exit, resulting in a more uniform near-field spray interacting with co- and atomisation airflow. This fuel placement uniformity provides the basis for the subsequent analysis of flame characteristics and emission behaviour.

4.3. Combustion characterisation

Time-averaged OH* chemiluminescence (OH*-CL) images together with the corresponding direct flame images are presented for the different injector configurations in Fig. 9. The conventional AB injector C1 (panel a) exhibits a radially distorted intensity distribution in the region $z = 50$–120 mm, followed by a downstream zone of high intensity exceeding 80% at approximately $z = 130$–180 mm, resulting in an elongated flame structure. Meanwhile, the high-intensity region of S1 (panel b) is broadened both radially and axially, while the initial flame anchoring occurs directly downstream of the nozzle edge. Increasing the fuel loading to $\dot{m}_l = 0.4$ g/s with $\Phi = 0.8$ (panel c) markedly widens the high OH*-CL region. The implementation of the μ-structure with a height of 40 μm at the airblast wall promotes asymmetry during the initial flame stages, shifting the anchoring point towards the nozzle and inwards. Notably, the S2 configuration exhibits only minor variations in droplet size and fuel loading distribution compared to S1, yet alters flame stabilisation. As summarised in Table 2, this behaviour is accompanied by reductions in Re_s and We_s, while the Oh remains comparable. This suggests that modifications in droplet–gas momentum coupling, rather than changes in primary atomisation characteristics, govern the redistribution of the near-field heat-release zone downstream of the injector in the μ-slit configuration. This tendency becomes more pronounced for the S3 configuration with the inner low swirler, which exhibits a more spatially uniform OH*-CL field with strong radial symmetry and a more compact flame shape.

In Fig. 10, the statistical response of the global flame lift-off height, $l_{loh,g}$, and the axial location of maximum OH* chemiluminescence, l_{max}, are evaluated for the C1 and S1 injectors across varying operating conditions at $T_j = 650$ K. Panel group (a) illustrates the influence of equivalence ratio Φ at fixed $u_j = 120$ m/s, while panel group (b) shows the effect of jet velocity. For the S1 injector, increasing Φ from 0.6 to 1.2 results in a decrease in $\bar{l}_{max}$ from 148 mm to 118 mm, accompanied by a 22% reduction in l'_{max}. A similar, yet rather marginal trend is observed in $\bar{l}_{loh,g}$, which decreases from 53.3 mm to 48.9 mm, also with a 17% reduction in $l'_{loh,g}$ to 3.01 mm. In contrast, the C1 injector exhibits a comparable $\bar{l}_{max}$ of 137 mm to that of S1, but shows substantially stronger fluctuations, reaching 35.6 mm under lean operation ($\Phi = 0.6$), which attenuate by approximately 50% at $\Phi = 1.0$. More notably, $\bar{l}_{loh,g}$ increases from 37.1 mm to 54.9 mm (approximately 48%) with increasing Φ, accompanied by a 10% reduction in $l'_{loh,g}$. The sensitivity to jet velocity ($u_j = 80$–160 m/s) further distinguishes the injector concepts. For S1, both $\bar{l}_{max}$ and $\bar{l}_{loh,g}$ remain nearly constant at 139 mm and 52.5 mm, respectively, whereas l'_{max} increases by approximately 110% with decreasing equivalence ratio and enhanced turbulent fluctuations. Conversely, the dual AB injector (C1) exhibits a substantial reduction in $\bar{l}_{loh,g}$ from 51.3 mm to 37.1 mm, accompanied by a consistent $l'_{loh,g}$ of 5.62 mm at elevated u_j up to 120 m/s. At higher jet velocities, the OH*–CL intensity becomes too weak for statistical evaluation. Overall, the μ-slit injector offers stable flame anchoring and a consistent location of the maximum reaction zone across the investigated operating conditions owing to the organised multi-phase mixture structure rather than variations in droplet size and velocity components.

Across the investigated operating range, the μ-slit configuration demonstrates comparatively stable flame anchoring and heat-release dynamics. To further examine the stabilisation behaviour, the spatial ignition onset locations from the left and right sides of the flame are shown for different injector configurations in Fig. 10(c). At an identical equivalence ratio of $\Phi = 0.6$, the C1 configuration exhibits median values of l_{loh} and $|x|_{loh}$ of 40.1 mm and 5.61 mm, respectively, indicating reaction onset close to the nozzle edge and exit, consistent with previous observations [34,47]. The ignition locations display a relatively large spatial fluctuation, with radial and axial spreads of 6.43 mm and 17.5 mm, respectively. This behaviour is associated with enhanced three-dimensional turbulence kinetic energy k and droplet intermittency near the nozzle edge, as shown in the SMM (Figs. S5 and S7). In contrast, the S1 configuration exhibits a lifted median l_{loh} of 55.6 mm while maintaining a similar median $|x|_{loh}$ of 5.67 mm. The spatial spreads of l_{loh} and $|x|_{loh}$ are reduced by 12% and 36%, respectively, relative to the C1 configuration. This suggests that the reaction onset guided by the airblast wall persists, while the simplified flow-guiding structure of the μ-slit injector suppresses turbulence fluctuations and promotes more stable flame anchoring. Introducing a low circumferential velocity in the co-flow for the S3 injector shifts l_{loh} upstream and increases the radial spread of $|x|_{loh}$ at 6.21 mm. The μ-bump-integrated configuration (S2) induces a further upstream and nozzle-inward shift of the anchoring location, with median values of $l_{loh} = 45.4$ mm and $|x|_{loh} = 3.76$ mm, while maintaining a moderate spatial spread of approximately 4.1 mm. However, it exhibits larger median left–right deviations in l_{loh} and $|x|_{loh}$ of 6.21 mm and 2.21 mm, respectively. This asymmetry may be associated with the radially biased axial velocity components shown in Fig. 6, while minor fabrication angle errors or alignment offsets may also contribute.

To further quantify flame stabilisation and structural asymmetry, statistical metrics are summarised in Table 3. The conventional injector (C1) exhibits smaller mean differences in flame anchoring coordinates, with $\overline{|\Delta l_{loh}|} = 0.12$ mm and $\overline{|\Delta x_{loh}|} = 0.29$ mm, compared with 1.48 mm and 0.48 mm for the S1 configuration, respectively, indicating slightly better geometric symmetry of the mean flame anchoring, yet with elevated temporal fluctuations. This difference becomes more pronounced with structural modifications, yielding values of 5.74 mm and 1.92 mm for the μ-bumps configuration (S2), and 2.61 mm and 1.11 mm for the low-swirl case (S3). In contrast, when considering the overall flame structure, the S1 configuration shows improvements of 32% (30%) and 16% (60%) in $\overline{A}_{\mathrm{asym}}$ (A'_{asym}) and $\overline{\psi}$ (ψ'), respectively, relative to the C1 configuration. Furthermore, the OH*-CL intensity-based Wasserstein distance $\overline{D}_{w1,I}$, exhibits reductions of 36% and 53% in the mean and fluctuations, respectively, with the introduction of the μ-slit injector. The S2 and S3 configurations maintain the structural symmetry characteristics of S1 while producing a more homogeneous heat-release intensity, with $\overline{D}_{w1,I}$ values of 0.14 and 0.11, respectively. Overall, the introduction of the μ-slit injector promotes more homogeneous fuel placement through the statistically isotropic circumferential topology of the μ-channels, leading to improved global symmetry and uniformity of the heat-release structure and intensity. Meanwhile, additional

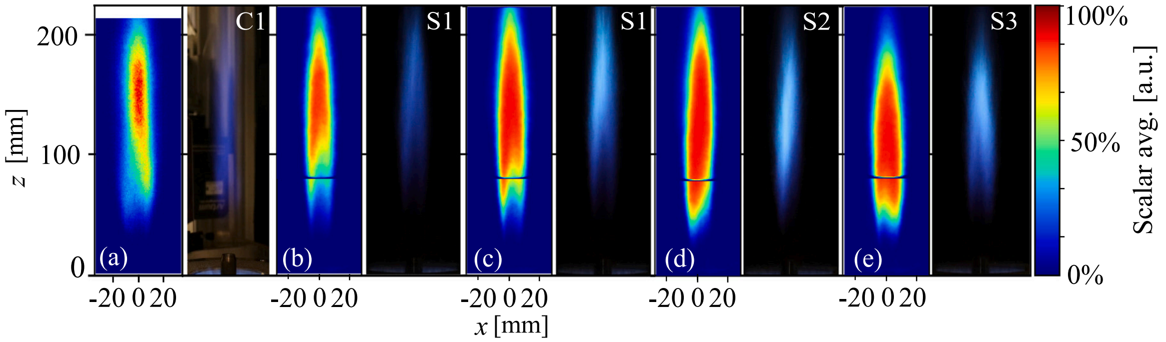

Fig. 9. Averaged OH*-CL images with direct flame imaging for various injector types. C1 (a) and S1 (b) are measured at $\dot{m}_l = 0.3\,\mathrm{g/s}$, $u_j = 120\,\mathrm{m/s}$, and $T_j = 650\,\mathrm{K}$. Panels (c) to (e) show measurements with conditions changed to $\dot{m}_l = 0.4\,\mathrm{g/s}$ with different injector types. Direct images are not intensity-scaled and are therefore not directly comparable between the C1 and S1 cases because they were acquired in different measurement campaigns.

Table 3

Summary of OH*-CL field asymmetry and similarity metrics for different injectors at fixed operating conditions ($u_j = 120\,\mathrm{m/s}$, $\dot{m}_l = 0.3\,\mathrm{g/s}$, and $\Phi = 0.6$). $\overline{|\Delta l_{loh}|}$ and $\overline{|\Delta x_{loh}|}$ represent the mean differences in the lift-off height and radial flame anchoring location, respectively. $\overline{A}_{\mathrm{asym}}$ and A'_{asym} denote the mean and standard deviation of the area asymmetry. $\overline{\psi}$ and ψ' indicate the mean and standard deviation of the normalised cross-correlation. $\overline{D}_{w1,I}$ and $D'_{w1,I}$ represent the mean and standard deviation of the OH*-CL intensity-based Wasserstein distance.

Metric	S1	S2	S3	C1
$\overline{\lvert\Delta l_{loh}\rvert}$ [mm]	1.48	5.74	2.61	0.12
$\overline{\lvert\Delta x_{loh}\rvert}$ [mm]	0.48	1.92	1.11	0.29
$\overline{A}_{\mathrm{asym}} \times 10$ [-]	0.40	0.42	0.51	0.59
$A'_{\mathrm{asym}} \times 10$ [-]	0.31	0.31	0.37	0.44
$\overline{\psi}$ [-]	0.87	0.83	0.87	0.75
ψ' [-]	0.04	0.05	0.04	0.10
$\overline{D}_{w1,I}$ [-]	0.16	0.14	0.11	0.25
$D'_{w1,I}$ [-]	0.07	0.06	0.06	0.15

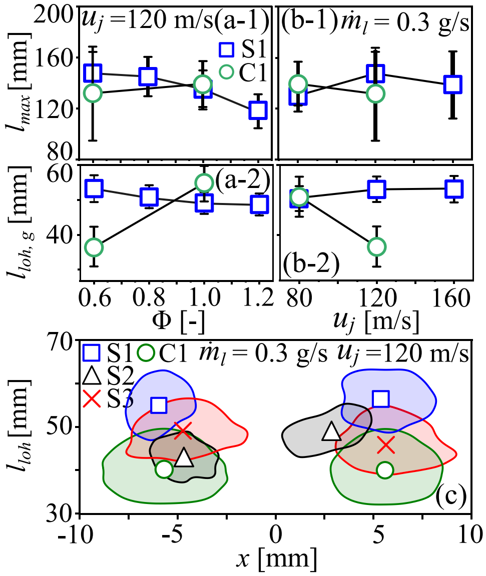

Fig. 10. Effects of Φ (panel group a) and u_j (panel group b) on the axial location of maximum OH*–CL intensity, l_{max}, and the global flame lift-off height, $l_{loh,g}$, for the S1 and C1 configurations. Symbols and error bars denote the mean and standard deviation. Panel (c) shows l_{loh} for different injector types at fixed operating conditions ($\dot{m}_l = 0.3\,\mathrm{g/s}$, $u_j = 120\,\mathrm{m/s}$, $T_j = 650\,\mathrm{K}$). Symbols indicate the median values, and the contours represent the third quartile of the distribution.

structural modifications, such as bumps and the swirler, slightly perturb the local flow and fuel-loading distribution and break the symmetry of flame anchoring, while still enhancing the overall uniformity of the reaction field. A similar tendency is observed under variations in jet velocity and equivalence ratio (see Table S3 in the SMM), confirming that the injector-dependent behaviour persists across operating conditions.

The flame stabilisation mechanism is further examined through the characteristic length scale of a droplet cluster, L_c, derived from Voronoi tessellation–based droplet spacing and normalised by d_{10}, evaluated at $x/D_c = 0$ and $x/D_c = 0.33$, obtained at $z/D_c = 2$ (Fig. 11(a-1 and a-2)), together with the corresponding cluster-driven group combustion number, G_v (Fig. 11(b)). The S3 configuration is excluded due to the limited statistical representativeness of the cluster-resolved quantities caused by the sparse and strongly evaporating droplet field. The conventional injector (C1) exhibits the smallest clustering length scale, with mean values of 570 and 620 at the two radial locations, whereas the µ-slit injectors produce substantially larger values, with mean L_c/d_{10} of 1712 (1377) for S1 and 1752 (1160) for S2 at $x/D_c = 0$ (0.33). This behaviour indicates that the slit-based geometries primarily modify the local droplet spacing within clusters rather than the mean droplet size itself. Although the large mean values of L_c/d_{10} indicate highly dilute droplet distributions, the relative differences among the injector concepts reflect changes in the local droplet-droplet interaction strength within the spray.

Fig. 11(b) presents the cluster-resolved group combustion number, G_v, along the radial locations for the conventional and µ-slit injector configurations. All measured cases exhibit values of comparable order to the classical group combustion number (see Fig. S2 in the SMM). The C1 injector consistently shows higher G_v values, reaching a maximum mean value of approximately 1.5×10^{-2} at $|x| = 4\,\mathrm{mm}$ ($|x|/D_c = 0.33$), close to the reaction onset location, with similarly elevated values of approximately 1.0×10^{-2} within the nozzle-core region ($|x| \leq 4\,\mathrm{mm}$). These higher values indicate reduced droplet spacing and enhanced local collective evaporation effects, suggesting a departure from purely isolated single-droplet behaviour rather than a fully developed internal

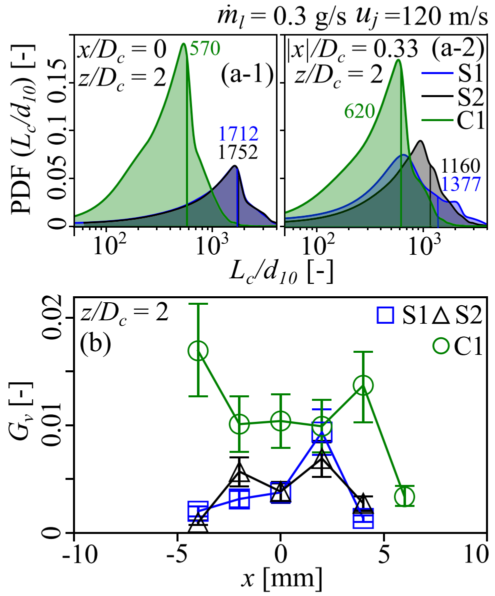

Fig. 11. Probability density functions of the normalised clustering length (L_c/d_{10}) at radial locations $x/D_c = 0$ (a-1) and $x/D_c = 0.33$ (a-2). Vertical lines indicate the mean value for each injector configuration. The S3 configuration is omitted because strong droplet evaporation results in an insufficient number of cluster samples for reliable statistics; consequently, the corresponding G_v values are not evaluated. Panel (b) presents the radial distribution of the cluster-resolved group combustion number G_v at $z/D_c = 2$. Symbols denote the median values, while the upper and lower bars represent the interquartile range (IQR).

group combustion regime [57]. At the same time, the larger radial variation and broader IQR-based spread of G_v, approximately 5.2×10^{-3} and about 2.6 times higher than that of S1, indicate a more intermittent local combustion environment that contributes to the broader spatial distribution of flame anchoring points. Such clustering-induced vapour enrichment can promote earlier ignition and upstream flame stabilisation, consistent with previous observations for evaporating droplet clusters [39,61].

In contrast, the μ-slit injectors exhibit the lowest G_v values near the nozzle edge, approximately 1.6×10^{-3} with a spread of approximately 1.0×10^{-3}, and higher values towards the nozzle interior, with an average of approximately 5.5×10^{-3}. These low G_v values indicate weak collective droplet interaction and evaporation behaviour approaching the isolated single-droplet limit, thereby promoting a more spatially distributed evaporation–mixing process. Together with the narrower spread, this behaviour is consistent with the spatially more confined flame anchoring observed for the μ-slit cases. Thus, flame stabilisation is strongly affected by injector-induced changes in droplet clustering and the resulting balance between collective and isolated droplet evaporation behaviour. It is worth noting that the S2 configuration exhibits slightly improved radial symmetry of G_v compared with S1 while maintaining a similar spread. The S3 configuration cannot be evaluated in terms of G_v due to the absence of statistically meaningful droplet clusters in the measurement region.

4.4. Injector performance

Revisiting the shadowgraphy images shown in Fig. 5 (a – c), increasing the air preheating temperature (T_j) diminishes the existence of droplets from the μ-slit injector due to vaporisation within the fuel plenum and nozzle exit. This phenomenon can also be observed through the pressure drop across the injector. Fig. 12(a) illustrates the pressure drop (ΔP) in relation to the air preheating temperature, jet velocity, and injector types. At a lower T_j of 350 K, ΔP increases with $\dot{m}_l$. At an intermediate T_j of 500 K, ΔP increases consistently with $\dot{m}_l$, yet at a significantly lower rate due to the enhanced heating of the liquid fuel and associated reduction in viscosity and surface tension. Upon increasing T_j to 650 K, ΔP rises up to 8 bar at a mass flow rate of 0.2 g/s and then decreases until $\dot{m}_l = 0.4$ g/s. At higher $\dot{m}_l$ the pressure drop increases again. This is attributed to pre-vaporisation within the fuel plenum due to heat transfer from the preheated air. This non-linear ΔP behaviour with respect to fuel flow rate is also observed for the jet velocity (u_j) variation ranging from 80 to 160 m/s, as shown in Fig. 12(b). Increasing u_j shifts the first maximum and minimum of ΔP during phase transition towards higher $\dot{m}_l$, resulting in higher ΔP values after the first peak, i.e., pre-vaporisation is occurring for a broadened $\dot{m}_l$ range. This highlights the need for further studies on the heat transfer mechanisms and design optimisation, as well as fuel properties in the current μ-slit type injector.

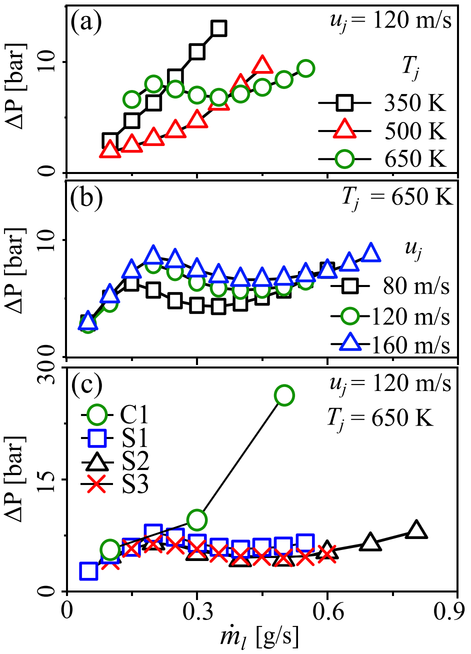

Fig. 12. Pressure drop (ΔP) across the fuel injector as a function of fuel mass flow rate for different air preheating temperatures (a), jet velocities (b), and injector types (c).

To observe the effects of fuel injection concepts and design parameters in terms of ΔP, Fig. 12(c) is presented. Due to the inherently small hole size (180 μm) of the PS injector, the C1 injector requires a 54% higher ΔP at 9.6 bar to inject fuel with $\dot{m}_l = 0.3$ g/s, compared with S1. Additionally, at a mass flow rate of $\dot{m}_l = 0.5$ g/s, ΔP substantially increases to 26 bar. However, for injectors S1 – S3, ΔP remains below a maximum of 8 bar across all $\dot{m}_l$ ranges, even with vaporisation. It is noteworthy that the inner-swirl and wall-film modification cases exhibit pressure drops similar to S1 ($R^2 = 0.92$), indicating consistent reproduction of the stochastic μ-channel connectivity (see SMM Fig. S3) and its corresponding dynamic response by the identical additive manufacturing process. Generally, the PS injector requires a higher pressure drop at the same fuel mass flow rate, yet increases exponentially under high fuel loading conditions, indicating higher hydraulic losses associated with the swirl chamber design. In contrast, the μ-slit injectors deliver the same fuel mass flow rate at substantially lower ΔP. The lower pressure requirement further enables a wider operational range and faster dynamic response, supporting scalability across different power ratings. These characteristics highlight the strong potential of the slit-injector concept for future hybrid aero-engines and micro gas turbine systems. However, it is noteworthy that long-term operation may

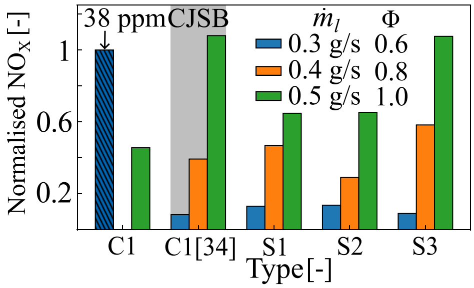

Fig. 13. Normalised NO_X emissions corrected to 15% O_2 for different injector configurations and liquid loading conditions at constant $u_j = 120$ m/s. The emissions are normalised using the C1 configuration at $\dot{m}_l = 0.3$ g/s ($\Phi = 0.6$), corresponding to approximately 38 ppm, as the reference condition, indicated by the hatched bar. Results are shown for $\dot{m}_l = 0.3$ g/s, 0.4 g/s, and 0.5 g/s ($\Phi = 0.6$–1.0), together with confined jet-stabilised combustor (CJSB) data from Ref. [34].

promote deposit accumulation and coking within the μ-slit channel, leading to a gradual increase in hydraulic resistance. Under representative operating conditions, the pressure drop increased by approximately 5%–10% after 2–10 h of operation. This trend is likely associated with thermally induced fuel decomposition under elevated thermal loading, particularly at high T_j and low $\dot{m}_l$, where locally reduced flow rates and stagnation-prone regions may promote deposit formation. Similar deposits can also be observed in the conventional pressure-swirl injector, suggesting that deposit formation is not unique to the μ-slit concept but is linked to the broader challenge of thermally loaded liquid-fuel injection. Such effects may be mitigated through improved thermal management and thermal isolation between the combustion air stream and liquid-fuel passages, facilitated by the geometric design freedom of additive manufacturing.

The normalised NO_X emissions, corrected to 15% O_2, are summarised in Fig. 13 for increasing liquid loading from $\dot{m}_l = 0.3$ g/s to 0.5 g/s ($\Phi = 0.6$–1.0) at constant $u_j = 120$ m/s. The emissions are normalised by the open C1 case at $\dot{m}_l = 0.3$ g/s, corresponding to approximately 38 ppm. The C1 case at $\dot{m}_l = 0.4$ g/s was not measured. At the lean condition, the open C1 configuration exhibits the highest NO_X level despite incomplete combustion with CO emissions exceeding 3300 ppm [40]. In contrast, the open μ-slit configurations reduce NO_X to approximately 5 ppm while maintaining CO below 30 ppm, indicating improved flame stabilisation through spatially distributed fuel discharge and enhanced near-field mixing, consistent with the stable flame anchoring observed for S1 in the SMM Fig. S9. The confined C1 combustor from Ref. [34] also shows reduced NO_X despite comparable atomisation characteristics ($d_{32} \approx 10$–15 μm), owing to confinement-assisted stabilisation and more complete combustion. With increasing liquid loading, NO_X increases monotonically for both the confined C1 combustor and the μ-slit configurations, reaching up to approximately 41 ppm. At $\Phi = 1.0$, the μ-slit cases exhibit higher normalised NO_X than the open C1 case, by approximately 40% for S1 and S2 and 135% for S3, while the absolute levels remain modest at approximately 24–40 ppm. This increase is attributed to enhanced combustion progress and stronger OH*-CL intensity, which is indicative of elevated peak-temperature regions [62], thereby promoting thermal NO_X formation, as shown in Fig. 9. Overall, the μ-slit injector enables stable low-NO_X combustion under lean conditions, while increasing liquid loading enhances combustion intensity and consequently thermal NO_X formation. Compared with C1, the μ-slit configuration exhibits reduced visible soot formation at $u_j = 80$ m/s and $\dot{m}_l = 0.3$ g/s, with no visible soot observed at $u_j = 120$ and 160 m/s even at increased equivalence ratio, as shown in the SMM Fig. S9.

5. Conclusions

This study demonstrates that additive manufacturing enables architecture-level control of liquid fuel injection through a continuous 50 μm annular slit topology inaccessible to conventional machining. μ-XRCT analysis confirms a manufacturable slit width of approximately 52 μm and reveals stochastic annular wall connectivity near the slit exit. This circumferentially redistributed exit topology modifies the local hydraulic resistance field and suppresses persistent sectoral fuel discharge bias.

As a direct consequence, the initial spray formation transitions from pressure-swirl-driven intermittent breakup towards intrinsically annular, spatially distributed microscale liquid sheets. The resulting injection topology promotes more homogeneous fuel placement with immediate droplet formation, reducing droplet size, radial asymmetry, and fuel-loading intermittency. These characteristics improve fuel-air mixing and reduce scatter in flame anchoring coordinates across a wide operating range. Additional structural modulation through μ-bumps and low-swirl flow introduces local perturbations in the flow field and fuel-loading distribution, slightly modifying local anchoring behaviour while maintaining globally symmetric flame structures.

Voronoi-resolved droplet clustering analysis and the corresponding group combustion number clarify the relative flame-stabilisation behaviour. Compared with C1, the μ-slit injectors show lower group combustion numbers and weaker collective droplet interaction, indicating evaporation behaviour closer to the isolated single-droplet limit and a more distributed evaporation–mixing process. Conversely, the higher values and broader spread observed for C1 suggest stronger local collective evaporation and vapour-enrichment tendencies, rather than a fully developed group-combustion regime. These differences are associated with a downstream, more stable flame anchoring of the μ-slit cases. Furthermore, the results highlight the importance of droplet–vapour–turbulence interaction and motivate future simultaneous scalar and velocity measurements, such as fuel-vapour laser-induced fluorescence combined with particle image velocimetry.

The μ-slit injector operates with a lower pressure drop than the reference pressure-swirl injector across all investigated operating conditions. However, the non-linear pressure trends indicate possible thermal interaction between the preheated co-flow and the μ-channel, potentially modifying liquid properties and atomisation behaviour while raising concerns regarding long-term fouling or coking. The resulting near-field spray topology and distributed evaporation process promote homogeneous heat release and stable low-NO_X combustion under lean conditions through improved fuel placement and enhanced mixing, while maintaining combustion completeness without excessive NO_X penalties over varying liquid loading conditions. The present findings demonstrate the potential for scalable, fuel-flexible, and low-emission combustor designs. In particular, the simple slit geometry, leveraged by additive manufacturing, enables fully integrated multi-nozzle configurations within a single build, potentially reducing assembly complexity, part count, and structural weight while supporting compact and cost-effective aero-engine and MGT combustors. Future investigations under elevated-pressure conditions and varying injector scales are required to assess pressure-dependent atomisation, thermo-mechanical robustness, stress loading, maintenance-related degradation, and long-term operational durability of the present μ-slit concept.

CRediT authorship contribution statement

Yeonse Kang: Writing – review & editing, Writing – original draft, Visualization, Methodology, Investigation, Formal analysis, Data curation. **Oliver Lammel:** Writing – review & editing, Resources, Funding acquisition. **Matthias Ruf:** Writing – review & editing, Data curation. **Holger Steeb:** Writing – review & editing, Resources, Funding acquisition. **Hans-Christian Möhring:** Writing – review & editing, Resources, Funding acquisition. **Fabian Hampp:** Writing – review & editing, Supervision, Resources, Project administration, Methodology, Funding acquisition, Conceptualization.

Declaration of competing interest

The authors declare that they have no known competing financial interests or personal relationships that could have appeared to influence the work reported in this paper.

Acknowledgements

The authors gratefully acknowledge funding from the Deutsche Forschungsgemeinschaft (DFG, German Research Foundation) under project numbers 456687251 (YK and FH) and 523873650 (HCM). The work of MR and HS is funded by the DFG, SFB 1313, project number 327154368, research projects Z02. YK and FH also acknowledge support from the Institute of Combustion Technology, DLR Stuttgart, and the Stuttgart Center for Simulation Science (SimTech).

Appendix A. Supplementary data

Supplementary material related to this article can be found online at https://doi.org/10.1016/j.jaecs.2026.100519.

Data availability

Data will be made available on request.

References

[1] Renewable energy targets. 2023, Available at https://energy.ec.europa.eu/topics/renewable-energy/renewable-energy-directive-targets-and-rules/renewable-energy-targets_en.

[2] Figini E, Paolone M. Achieving dispatchability in data centers: Carbon and cost-aware sizing of energy storage and local photovoltaic generation. Sustain Energy Grids Netw 2025;43:101920.

[3] Liang S. Research on data center load simulation and optimization of integrated energy system. AIP Adv 2025;15:085003.

[4] Wärtsilä. Data centre dispatchable capacity: a major opportunity for Europe's energy transition. 2025, Available at https://www.wartsila.com/docs/default-source/energy-docs/technology-products/white-papers/data-centre-dispatchable-capacity-avk-wartsila_white-paper_2025.pdf.

[5] Moliére M. The fuel flexibility of gas turbines: A review and retrospective outlook. Energies 2023;16:3962.

[6] Huth M, Heilos A. Fuel flexibility in gas turbine systems: impact on burner design and performance. In: modern gas turbine systems. Woodhead Publishing; 2013, p. 635–84.

[7] Mitsubishi Power. Meeting data center demand. 2024, Available at https://power.mhi.com/regions/amer/insights/meeting-data-center-demand.

[8] Gebisa AW, Lemu HG. Additive manufacturing for the manufacture of gas turbine engine components: Literature review and future perspectives. Proc ASME Turbo Expo 2018;GT2018–76686.

[9] Pereira T, Kennedy J, Potgieter J. A comparison of traditional manufacturing vs additive manufacturing, the best method for the job. Procedia Manuf 2019;30:11–8.

[10] Sun C, Wang Y, McMurtrey M, Jerred N, Liou F, Li J. Additive manufacturing for energy: A review. Appl Energy 2021;282:116041.

[11] Giuliani F, Paulitsch N, Cozzi D, Görtler M, Andracher L. An assessment on the benefits of additive manufacturing regarding new swirler geometries for gas turbine burners. Proc ASME Turbo Expo 2018;GT2018–75165.

[12] Rajasegar R, Mitsingas CM, Mayhew EK, Liu Q, Lee T, Yoo J. Development and characterization of additive-manufactured mesoscale combustor array. J Energy Eng 2018;144:04018013.

[13] Kim S, Kim J, Byun H, Ku JW, Do H, Kwak S, Han D, Jung S, Park H. Development of a novel hydrogen burner using additive manufacturing. Proc ASME Turbo Expo 2024;GT2024–123608.

[14] Durocher A, Fan L, Francolini B, Füri M, Bourque G, Sirois J, May D, Bergthorson JM, Yun S, Vena P. Characterization of a novel additive manufacturing micromix nozzle burning methane to hydrogen. J Eng Gas Turbines Power 2024;146:051009.

[15] Rubio V, Ahn J, Maucher C, Möhring H-C, Hampp F. AM enabled injection systems for enhanced fuel flexibility. E3S Web Conf 2025;663:01012.

[16] Guddati S, Kiran ASK, Leavy M, Ramakrishna S. Recent advancements in additive manufacturing technologies for porous material applications. Int J Adv Manuf Technol 2019;105:193–215.

[17] Crayford A, Lacan F, Runyon J, Bowen P, Balwadkar S, Harper J, Pugh D. Manufacture, characterization and stability limits of an AM prefilming air-blast atomizer. Proc ASME Turbo Expo 2019;GT2019–91624.

[18] Adamou A, Kennedy I, Farmer B, Hussein A, Copeland C. Experimental and computational analysis of an additively manufactured vaporization injector for a micro-gas turbine. Proc ASME Turbo Expo 2019;GT2019–90245.

[19] Kang Y, Jose B, Hampp F. Pushing fuel flexibility with AM μ-slit injector for jet-stabilised combustion. Int J Spray Combust Dyn 2026;18:26–40.

[20] Moon S, Choi J, Yeom K, Bae C. Measurements of droplet size distribution and in-cylinder mixture formation from a slit injector in a direct-injection gasoline engine. J Phys: Conf Ser 2007;85:012004.

[21] Mo GU, Koo IH, Lee K-H, Choi S-W, Choi J-Y. Effects of fuel penetration on the RDE performance with JISC injector configuration. Aerosp 2024;11:752.

[22] Heo S, Jeong J, Yoon Y. Spray characteristics of a multi-slit type throttleable pintle injector with different slit heights. Acta Astronaut 2024;215:475–92.

[23] Fruzza F, Chu H, Lamioni R, Grenga T, Galletti C, Pitsch H. Three-dimensional numerical investigation of flashback in premixed hydrogen flames within perforated burners. Combust Flame 2025;274:113987.

[24] Díaz A, Alegre JM, Cuesta II, M.-Peñeda E. A COMSOL framework for predicting hydrogen embrittlement, part II: Phase field fracture. Eng Fract Mech 2025;319:111008.

[25] Vance FH, de Goey LPH, van Oijen JA. Development of a flashback correlation for burner-stabilized hydrogen-air premixed flames. Combust Flame 2022;243:112045.

[26] Lee T, Kim KT. High-frequency transverse combustion instabilities of lean-premixed multislit hydrogen-air flames. Combust Flame 2022;238:111899.

[27] Lefebvre AH, McDonell VG. Atomization and sprays. 2nd ed. CRC Press; 2017.

[28] Sattelmayer T, Wittig S. Internal flow effects in prefilming airblast atomizers: Mechanisms of atomization and droplet spectra. J Eng Gas Turbines Power 1986;108:465–72.

[29] Sattelmayer T, Wittig S. Performance characteristics of prefilming atomizers in comparison with other airblast atomizers. In: Encyclopedia of fluid mechanics, vol. 8, Gulf Publishing Company; 1986, p. 1091–141.

[30] Bhayaraju UC. Analysis of liquid sheet breakup and characterisation of plane prefilming and nonprefilming airblast atomisers [Ph.D. thesis], Darmstadt, Germany: Technische Universität Darmstadt; 2007.

[31] Kumar A, Sahu S. Liquid jet breakup unsteadiness in a coaxial air-blast atomizer. Int J Spray Combust Dyn 2018;10:211–30.

[32] Petry N, Mannazhi M, Yin Z, Lammel O, Geigle KP, Huber A. Investigation of fuel and load flexibility of an atmospheric single nozzle jet-stabilized FLOX combustor with hydrogen/methane-air mixtures. J Eng Gas Turbines Power 2024;146:061004.

[33] Lammel O, Severin M, Ax H, Lückerath R, Tomasello A, Emmi Y, Noll B, Aigner M, Panek L. High momentum jet flames at elevated pressure, A: Experimental and numerical investigation for different fuels. Proc ASME Turbo Expo 2017;GT2017–64615.

[34] Hampp F, Schäfer D, Lammel O. Spray flame characterization of a dual injector for compact combustion systems. Comb Sci Tech 2023;197:463–96.

[35] Zanger J, Monz T, Aigner M. Experimental investigation of the combustion characteristics of a double-staged FLOX®-based combustor on an atmospheric and a micro gas turbine test rig. Proc ASME Turbo Expo 2015;GT2015–42313.

[36] Seliger H, Huber A, Aigner M. Experimental investigation of a FLOX®-based combustor for a small-scale gas turbine based CHP system under atmospheric conditions. Proc ASME Turbo Expo 2015;GT2015–43094.

[37] Wünning J. Flameless oxidation to reduce thermal NO formation. Prog Energy Combust Sci 1997;23:81–94.

[38] Schmitz O, et al. Aero engine concepts beyond 2030: Part 3-experimental demonstration of technological feasibility. J Eng Gas Turbines Power 2021;143:021003.

[39] Hampp F, Schäfer D, Lammel O. Spray flame characterisation under lean blow-out conditions. Combust Flame 2024;268:113623.

[40] Kang Y, Ahn J, Hampp F. Low swirl effect on compact spray and combustion systems using additive manufactured dual airblast injectors. J Eng Gas Turbines Power 2024;146:121001.

[41] Kim H, Pareja J, Lammel O. Effects of a 3D-printed atomizer component on fuel-spray and flame characteristics of a jet-stabilized compact gas turbine combustor fed with liquid fuels. J Eng Gas Turbines Power 2024;146:121020.

[42] Moon S, Abo-Serie E, Bae C. Air flow and pressure inside a pressure-swirl spray and their effects on spray development. Exp Therm Fluid Sci 2009;33:222–31.

[43] Chen X, Yang V. Effect of ambient pressure on liquid swirl injector flow dynamics. Phys Fluids 2014;26:102104.

[44] Siamas GA, Jiang X, Wrobel LC. Dynamics of annular gas–liquid two-phase swirling jets. Int J Multiph Flow 2009;35:450–67.

[45] Belhadef A, Vallet A, Amielh M, Anselmet F. Pressure-swirl atomization: Modeling and experimental approaches. Int J Multiph Flow 2012;39:13–20.

[46] Petry N, Schäfer D, Lammel O, Hampp F. Quantification of coflow effects on primary atomization of pressure swirl atomizers. Int J Multiph Flow 2022;149:103946.

[47] Kang Y, Hampp F. Low-swirl effects on spray flames for compact jet-stabilised combustion systems. Combust Flame 2026;285:114740.

[48] Gillani SE, Al-Abdeli YM. Insights into the intrinsic asymmetry of bluff-body stabilised swirling and non-swirling annular flows. Exp Therm Fluid Sci 2024;150:111063.

[49] Izadi S, Zanger J, Kislat O, Enderle B, Grimm F, Kutne P, Aigner M. Experimental investigation of the combustion behavior of single-nozzle liquid-FLOX-based burners on an atmospheric test rig. J Eng Gas Turb. Power 2021;143:071021.

[50] Kang Y, Seidler J, Ahn J, Rubio V, Maucher C, Möhring H, Hampp F. AM micro-structures with bespoke permeability. Int J Heat Mass Transfer 2024;241:126674.

[51] Bell JH, Mehta RD. Contraction design for small wind tunnels (no. 177488). Washington, DC: NASA; 1988.

[52] Jia Q, Gu D. Selective laser melting additive manufacturing of Inconel 718 superalloy parts: Densification, microstructure and properties. J Alloys Compd 2014;585:713–21.

[53] Ruf M, Steeb H. An open, modular, and flexible micro X-ray computed tomography system for research. Rev Sci Instrum 2020;91:113102.

[54] Pandurangan N, Sahu S. Analysis of group evaporation characteristics of droplet clusters in an evaporating spray. J Fluid Mech 2024;998:A26.

[55] Mora-Paiba D. Clustering and settling dynamics of inertial particles under turbulence [Ph.D. thesis], Université Grenoble Alpes; 2020.

[56] Chiu H, Liu T. Group combustion of liquid droplets. Combust Sci Technol 1977;17:127—-142.

[57] Akamatsu F, Miutani Y, Katsuki M, Tsushima S, Cho YD. Measurement of the local group combustion number of droplet clusters in a premixed spray stream. Proc Combust Inst 1996;26:1723–9.

[58] Savard B, Blanquart G. An a priori model for the effective species Lewis numbers in premixed turbulent flames. Combust Flame 2014;161:1547–57.

[59] Maucher C, Kang Y, Bechler S, Ruf M, Steeb H, Möhring H, Hampp F. Towards bespoke gas permeability by functionally graded structures in laser-based powder bed fusion of metals. Addit Manuf 2024;94:104466.

[60] Konstantin K, Thomas K, Philipp T, Mathis B, Heinz P. Computational study of flame characteristics of a turbulent piloted jet burner with inhomogeneous inlets. Proc Combust Inst 2017;36:1747–57.

[61] Sirignano WA. Advances in droplet array combustion theory and modeling. Prog Energ Combust Sci 2014;42:54–86.

[62] Lauer M. Determination of the heat release distribution in turbulent flames by chemiluminescence imaging [Ph.D. thesis], Technische Universität München; 2011.